EUROPEAN ORGANISATION FOR NUCLEAR RESEARCH (CERN)

Submitted to: JHEP

CERN-EP-2022-054
24th June 2022

Search for light long-lived neutral particles that decay to collimated pairs of leptons or light hadrons in pp collisions at $\sqrt{s} = 13$ TeV with the ATLAS detector

The ATLAS Collaboration

A search for light long-lived neutral particles with masses in the O(MeV–GeV) range is presented. The analysis targets the production of long-lived dark photons in the decay of a Higgs boson produced via gluon–gluon fusion or in association with a W boson. Events that contain displaced collimated Standard Model fermions reconstructed in the calorimeter or muon spectrometer are selected in 139 fb^{-1} of $\sqrt{s} = 13$ TeV pp collision data collected by the ATLAS detector at the LHC. Background estimates for contributions from Standard Model processes and instrumental effects are extracted from data. The observed event yields are consistent with the expected background. Exclusion limits are reported on the production cross-section times branching fraction as a function of the mean proper decay length $c\tau$ of the dark photon, or as a function of the dark-photon mass and kinetic mixing parameter that quantifies the coupling between the Standard Model and potential hidden (dark) sectors. A Higgs boson branching fraction above 1% is excluded at 95% CL for a Higgs boson decaying into two dark photons for dark-photon mean proper decay lengths between 10 mm and 250 mm and dark photons with masses between 0.4 GeV and 2 GeV.

1 Introduction

Dark sectors weakly coupled to the Standard Model (SM) are predicted in several theories of physics beyond the Standard Model (BSM) [1–4]. Such theories often include a complex spectrum of new particles that form the dark sector and can couple to the SM only via specific portals. Depending on the structure of the dark sector and its coupling to the SM, unstable dark states may be produced at colliders, and could decay into SM particles with sizeable branching fractions.

This paper investigates the case where the SM and dark sectors communicate through the Higgs portal for the production of the BSM states and through a vector portal for the decay of the produced particles. In particular, a dark photon (γ_d) is assumed to mix kinetically with the SM photon and decay into leptons and light quarks [5–7]. The kinetic mixing parameter (ϵ), which is theoretically allowed to vary over a wide range of values, determines the lifetime of the dark photon. This analysis focuses on small values of the kinetic mixing parameter, $\epsilon < 10^{-5}$, corresponding to γ_d decays happening at a macroscopic distance from their production point, and a dark-photon mass in the O(MeV–GeV) range. The decay branching fractions of a light dark photon that mixes kinetically with the SM photon depend on its mass [6, 8, 9]. Due to their small mass compared to the energy scale of the hard-scattering process, the dark photons are expected to be produced with large Lorentz boosts, resulting in collimated groups of fermions in a jet-like structure, referred to hereafter as dark-photon jets (DPJs).

Two mutually exclusive search categories, referred to as *gluon–gluon fusion selection* and *WH associated production selection*, are designed to target the production of dark photons in these two Higgs boson production modes. Two models are used for the optimisation of the event selections and the interpretation of the final results: the Falkowski–Ruderman–Volansky–Zupan (FRVZ) model [6, 7] and the Hidden Abelian Higgs Model (HAHM) [4]. In the FRVZ model, a pair of dark fermions f_d is produced via a Higgs boson decay and can lead to final states with either two (Figure 1(a)) or four (Figure 1(b)) dark photons. In the two dark photon case, f_d decays into a dark photon and a stable dark fermion, which is assumed to be the hidden lightest stable particle (HLSP). Whereas in the four dark photon case, f_d decays into an HLSP and a dark scalar s_d that in turn decays into a pair of γ_d. The HAHM model predicts a direct decay of the Higgs boson into a pair of γ_d, as shown in Figure 1(c). The mean proper lifetime τ of the γ_d is inversely related to the mass of the dark photon and to the square of the kinetic mixing parameter [9, 10].

In general, dark-sector radiation [11] can produce extra dark photons proportionally to the size of the dark gauge coupling α_d [5]. In this work a dark coupling $\alpha_\mathrm{d} \lesssim 0.01$ is assumed, leading to no significant additional γ_d emission. For this reason, no specific interpretations are given for these scenarios.

The search for displaced DPJs presented in this paper uses the dataset collected at the Large Hadron Collider (LHC) by the ATLAS detector during 2015–2018 in proton–proton (pp) collisions at a centre-of-mass energy $\sqrt{s} = 13$ TeV, corresponding to an integrated luminosity of 139 fb^{-1}. Previous searches for displaced DPJs were performed by ATLAS using proton–proton collision data at lower centre-of-mass energies [12, 13] or a partial dataset corresponding to 36.1 fb^{-1} of proton–proton collision data at a centre-of-mass energy of $\sqrt{s} = 13$ TeV [14]. The results are complementary to those from related ATLAS searches for prompt DPJs [15–17], which probed higher values of ϵ, and for displaced dimuon vertices using 13 TeV data [18], which probed higher dark-photon mass values. Related searches for dark photons were conducted by the CDF and D0 collaborations at the Tevatron [19–21] and by the CMS [22–25] and LHCb [26, 27] collaborations at the LHC. Additional constraints on scenarios with dark photons are extracted from, e.g., beam-dump and fixed-target experiments [28–38], e^+e^- colliders [39–47], electron and muon anomalous magnetic moment measurements [48–50] and astrophysical observations [51, 52]. Given the various

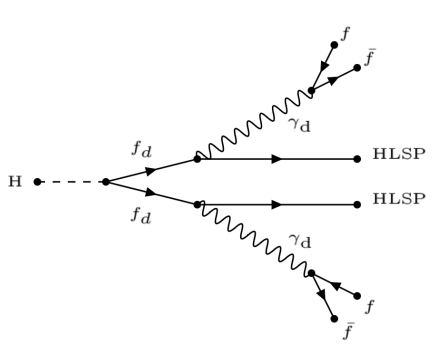

(a) FRVZ $2\gamma_d$

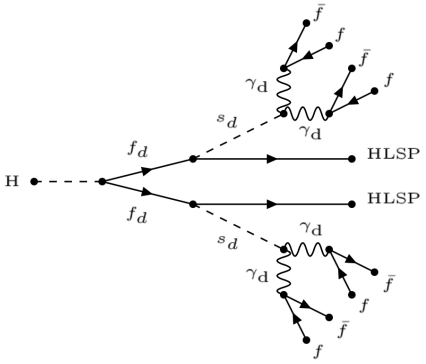

(b) FRVZ $4\gamma_d$

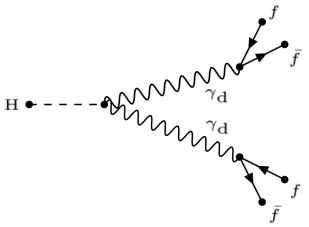

(c) HAHM $2\gamma_d$

Figure 1: (a) FRVZ process with the dark fermion f_d decaying into a γ_d and an HLSP. (b) FRVZ process with the dark fermion f_d decaying into an HLSP and a dark scalar s_d that in turn decays into a pair of dark photons. (c) HAHM process with the two γ_d directly produced by the Higgs boson (H). The γ_d decays into SM fermions, denoted by f and $\bar{f}$.

constraints, a displaced dark-photon decay with a kinetic mixing parameter $\epsilon < 10^{-5}$ is allowed for γ_d masses greater than 10 MeV. In this paper, the sensitivity to displaced DPJs is significantly higher than in the previous ATLAS search [14], due to the higher integrated luminosity of the dataset and to new analysis methods. The new analysis methods include updated signal-region selection criteria and DPJ reconstruction techniques. Multivariate techniques based on convolutional neural networks, exploiting the three-dimensional representations of calorimeter energy deposits associated with jets, and a dense neural network, using muon track information, are employed to indentify DPJ candidates. The addition of a new set of event selection criteria, targeting events where the dark photons arise from the decay of a scalar particle produced in association with a W boson, significantly increases the sensitivity in scenarios with γ_d mean proper decay lengths $c\tau$ below (above) 3 (40) mm.

2 ATLAS detector

The ATLAS detector [53] at the LHC covers nearly the entire solid angle around the collision point.[1] It consists of an inner tracking detector (ID) surrounded by a thin superconducting solenoid, electromagnetic (EM) and hadron (HCAL) calorimeters, and a muon spectrometer (MS) incorporating three large superconducting air-core toroidal magnets.

The inner tracking detector covers the pseudorapidity range $|\eta| < 2.5$. It consists of silicon pixel, silicon microstrip, and transition radiation tracking detectors.

The calorimeter system covers the pseudorapidity range $|\eta| < 4.9$. Within the region $|\eta| < 3.2$, electromagnetic calorimetry is provided by barrel and endcap high-granularity lead/liquid-argon (LAr) calorimeters, with an additional thin LAr presampler covering $|\eta| < 1.8$ to correct for energy loss in material upstream of the calorimeters. Hadron calorimetry is provided by the steel/scintillator-tile calorimeter, segmented into a central barrel and two extended-barrel cylindrical structures within $|\eta| < 1.7$, and two copper/LAr hadron endcap calorimeters. The solid angle coverage is completed with forward copper/LAr and tungsten/LAr calorimeter modules optimised for electromagnetic and hadronic energy measurements respectively. Overall, the calorimeter system is highly segmented in shower depth, with a total of seven sampling layers in the barrel region and eight in the endcap regions.

The muon spectrometer comprises separate trigger and high-precision tracking chambers measuring the deflection of muons in a magnetic field generated by the superconducting air-core toroidal magnets. The field integral of the toroids ranges between 2.0 and 6.0 T m across most of the detector. A set of precision chambers covers the region $|\eta| < 2.7$ with three layers of monitored drift tubes, complemented by cathode-strip chambers in the forward region, where the background is highest. The muon trigger system covers the range $|\eta| < 2.4$ with resistive-plate chambers in the barrel, and thin-gap chambers in the endcap regions.

A two-level trigger system is used to select events [54]. The first-level (L1) trigger is implemented in hardware and uses a subset of the detector information to accept events at a rate of at most 100 kHz. This is followed by a software-based high-level trigger (HLT) that reduces the accepted event rate to 1 kHz on average, depending on the data-taking conditions.

An extensive software suite [55] is used in the reconstruction and analysis of real and simulated data, in detector operations, and in the trigger and data acquisition systems of the experiment.

3 Data and simulated event samples

The data were collected by the ATLAS detector during Run 2 of the LHC (2015–2018) with a peak instantaneous luminosity of 2.1×10^{34} cm^{-2}s^{-1}, resulting in a mean number of pp interactions per bunch crossing of $\langle\mu\rangle = 34$. Data quality requirements [56] are applied to ensure that all subdetectors were operating normally, and that the LHC beams were in stable-collision mode. The integrated luminosity of the resulting data sample is 139 fb^{-1}. The data were collected using a set of triggers specifically

[1] ATLAS uses a right-handed coordinate system with its origin at the nominal interaction point (IP) in the centre of the detector and the z-axis along the beam pipe. The x-axis points from the IP to the centre of the LHC ring, and the y-axis points upwards. Cylindrical coordinates (r, ϕ) are used in the transverse plane, ϕ being the azimuthal angle around the z-axis. The pseudorapidity is defined in terms of the polar angle θ as $\eta = -\ln\tan(\theta/2)$, and the rapidity is defined as $y = (1/2)[(E + p_z)/(E - p_z)]$.

designed to target the displaced γ_d decays, described in detail in Section 5.1, or single-lepton triggers, with requirements on the identification, isolation, and p_T of the leptons to maintain efficiency across the full momentum range while controlling the trigger rates [57, 58].

During pp collisions data-taking the LHC circulates two counter-rotating proton beams constructed from bunches of protons. However, following LHC injection not all bunch slots are filled with protons, with the number of unfilled bunches depending on the LHC filling scheme [59]. An empty bunch crossing takes place when neither beam is filled with protons and each empty bunch is separated from filled bunches by at least five empty bunches on each side. A dataset enriched in cosmic-ray muon background is collected during empty bunch crossings (the 'cosmic dataset') and used for the background estimation.

Monte Carlo (MC) simulated event samples are used to model the BSM signals. Signal samples modelling the production of dark photons via a 125 GeV Higgs portal were generated with MadGraph5_aMC@NLO 2.2.3 [60] interfaced to Pythia 8.186 [61] for the parton showering (PS) and hadronisation. The matrix-element calculation was performed at tree level. The parton distribution function (PDF) set used for the generation is NNPDF2.3LO [62]. Higgs boson production via gluon–gluon fusion and in association with a W boson is included. The predicted Standard Model cross-sections for these two processes, assuming $m_H = 125.09$ GeV, are respectively 48.61 pb [63, 64] and 1.369 pb [65, 66]. A second set of signal samples was generated, modelling the production via gluon–gluon fusion of a high-mass (800 GeV) Higgs-like scalar mediator with the same decay modes as in the 125 GeV mass case. Effects of higher-order QCD corrections on the p_T of the Higgs boson, evaluated using a reweighting procedure [67], change the signal selection efficiency by less than the MC statistical accuracy and are therefore neglected. A dark photon with a mass m_{γ_d} up to a few GeV that mixes kinetically with the SM photon will decay into leptons or light quarks, with branching fractions that depend on its mass [6, 8, 9]. Taking as an example a dark-photon mass of 0.4 GeV, the γ_d decay branching ratios are expected to be 45% e^+e^-, 45% $\mu^+\mu^-$, and 10% $q\bar{q}$ [6]. The mean proper decay length $c\tau$ of the γ_d is a free parameter of the model. In the generated samples, $c\tau$ was chosen such that, accounting for the boost of the γ_d, a large fraction of the decays occur inside the sensitive ATLAS detector volume (i.e. up to 7 m in radius and 13 m along the z-axis from the centre of the detector). The decays of the Higgs boson into dark photons through dark fermions or directly into two dark photons were simulated at matrix-element level during the generation. In the FRVZ model, the mass of f_d was chosen to be small relative to the Higgs boson mass, and far from the kinematic threshold at $m_{\text{HLSP}} + m_{\gamma_d} = m_{f_d}$. In the HAHM, the Higgs boson decays directly into two dark photons.

The SM background is estimated using data-driven techniques, with MC simulated events used to aid in the validation, the evaluation of uncertainties, and the training of dedicated multivariate classifiers. SM processes that could be potential sources of background include multi-jet, W+jets, Z+jets, $t\bar{t}$, single-top-quark, WW, WZ, and ZZ production. The multi-jet samples were generated with Pythia 8.210 [68] using the same set of tuned parameter values (tune) and PDF as for the signal samples. Samples of W+jets, Z+jets, WW, WZ, and ZZ events were generated using Sherpa 2.2.1 [69] with the NNPDF3.0NNLO [70] PDF set. Single-top and $t\bar{t}$ MC samples were generated using Powheg Box v2 [71] and Pythia 8.230 with the A14 tune [72] for parton showering and hadronisation, and the NNPDF2.3LO set of PDFs.

Finally, MC samples of $J/\psi \to \mu\mu$ events were generated and used to evaluate systematic uncertainties for muon trigger and reconstruction efficiencies. The MC samples were generated using Pythia8+Photos++ [73] with the A14 tune for parton showering and hadronisation, and the CTEQ6L1 [74, 75] PDF set.

All generated Monte Carlo events were processed through a full simulation of the ATLAS detector geometry and response [76] using the Geant4 [77] toolkit. The simulation includes multiple pp interactions per

bunch crossing (pile-up), as well as the detector response to interactions in bunch crossings before and after the one producing the hard interaction. In order to model the effects of pile-up, simulated inclusive pp events were overlaid on each generated hard-scatter event and reweighted to match the conditions of the 2015–2018 data sample. The inclusive pp events were simulated with Pythia 8.210 with the A3 tune [78] and the NNPDF2.3lo set of PDFs.

4 Event reconstruction

Candidate events are required to have a reconstructed vertex [79] with at least two associated tracks with transverse momentum (p_{T}) larger than 500 MeV that are consistent with originating from the beam collision region in the x–y plane. The primary vertex in the event is the vertex with the highest sum of squared transverse momenta of associated tracks.

Electron candidates are reconstructed from isolated electromagnetic calorimeter energy deposits matched to ID tracks. They are required to have $|\eta| < 2.47$, a transverse momentum $p_{\mathrm{T}} > 20\,\mathrm{GeV}$, and to satisfy the 'TightLHElectron' requirement defined in Ref. [80], which is based on a likelihood evaluated using measurements of shower shapes in the calorimeter and track properties in the ID as input variables. Candidates within the transition region between the barrel and endcap electromagnetic calorimeters, $1.37 < |\eta| < 1.52$, are not considered.

Muon candidates are reconstructed in the region $|\eta| < 2.5$ from MS tracks matching ID tracks. They are required to have $p_{\mathrm{T}} > 20\,\mathrm{GeV}$ and satisfy the 'medium' identification requirements defined in Ref. [81]. These requirements are based on the number of hits in the different ID and MS subsystems, and on the ratio of the charge and momentum (q/p) measured in the ID and MS divided by the sum in quadrature of their corresponding uncertainties.

The tracks associated with the electron and muon candidates are required to have a significance of the transverse impact parameter,[2] d_0, of $|d_0|/\sigma(d_0) < 5$ for electrons and $|d_0|/\sigma(d_0) < 3$ for muons, and a longitudinal impact parameter, z_0, satisfying $|z_0 \sin\theta| < 0.5$ mm.

Isolation criteria are applied to electrons and muons. The scalar sum of the p_{T} of tracks within a variable-size cone around the electron (muon), must be less than 15% of the lepton p_{T}, excluding tracks associated with the lepton. The track isolation cone size for electrons (muons) $\Delta R = \sqrt{(\Delta\eta)^2 + (\Delta\phi)^2}$ is given by the smaller of $\Delta R = 10\ \mathrm{GeV}/p_{\mathrm{T}}$ and $\Delta R = 0.2$ (0.3). In addition, the sum of the transverse energy of clusters of calorimeter cells [82] in a cone of $\Delta R = 0.2$ around the electron (muon) must be less than 20% (30%) of the lepton p_{T}, excluding clusters associated with the lepton.

Jets are reconstructed from three-dimensional energy clusters in the calorimeter [83] using the anti-k_t jet clustering algorithm [84, 85] with a radius parameter $R = 0.4$. Only jet candidates with $p_{\mathrm{T}} > 20\,\mathrm{GeV}$ and $|\eta| < 4.9$ are considered. Jets are calibrated using MC simulation, with corrections obtained from in situ techniques [86]. To reduce the effects of pile-up, jets with $p_{\mathrm{T}} < 120\,\mathrm{GeV}$ and $|\eta| < 2.5$ are required to have a significant fraction of their associated tracks compatible with originating from the primary vertex, as defined by the jet vertex tagger [87] (JVT). This requirement reduces the fraction of jets from pile-up to

[2] The transverse impact parameter, d_0, is defined as the distance of closest approach of a track to the beam-line, measured in the transverse plane. The longitudinal impact parameter, z_0, corresponds to the z-coordinate distance between the point along the track at which the transverse impact parameter is defined and the primary vertex.

1%, with an efficiency for hard-scatter jets of about 90%. Jets not satisfying basic quality criteria designed to reject detector noise and non-collision backgrounds [88] are then discarded.

Jets containing b-hadrons (b-tagging) are identified with a multivariate discriminant that makes use of track properties [89, 90]. Jets are considered to be b-tagged if they fulfil a requirement that has 70% average efficiency for jets containing b-hadrons in simulated $t\bar{t}$ events. The rejection factors for light-quark and gluon jets, jets containing c-hadrons, and hadronically decaying τ-leptons in simulated $t\bar{t}$ events are approximately 301, 38, and 8, respectively.

Simulated events are corrected for differences from collision data in b-tagging efficiencies and b-tagging mis-tag rates [90–92]. Corrections are also applied to account for minor differences between data and MC simulation in the single-lepton trigger, reconstruction, identification and isolation efficiencies [93, 94].

Jet candidates within an angular distance $\Delta R' = \sqrt{(\Delta y)^2 + (\Delta\phi)^2} = 0.2$ of a lepton candidate are discarded. Remaining lepton candidates within $\Delta R' = \min\{0.4, 0.04 + p_{\mathrm{T}}(\mu)/(10\,\mathrm{GeV})\}$ of a jet are then discarded to suppress bottom and charm hadron decays. When considering muons, if the jet has fewer than three associated tracks, the muon is retained and the jet is discarded instead to avoid inefficiencies for high-energy muons undergoing significant energy loss in the calorimeter. Finally, any electron candidate sharing an ID track with a remaining muon candidate is also removed.

The missing transverse momentum vector $\mathbf{p}_{\mathrm{T}}^{\mathrm{miss}}$, whose magnitude is denoted by $E_{\mathrm{T}}^{\mathrm{miss}}$, is defined as the negative vector sum of the transverse momenta of all identified electrons, muons and jets, plus an additional soft term. The soft term is constructed from all tracks that originate from the primary vertex but are not associated with any identified lepton or jet. In this way, the $E_{\mathrm{T}}^{\mathrm{miss}}$ is adjusted for the best calibration of leptons and jets, while contributions from pile-up interactions are suppressed through their exclusion from the soft term [80, 81].

A displaced γ_{d} decay producing a pair of muons is expected to leave two or more collimated stand-alone MS tracks, referred to as a muonic dark-photon jet μDPJ. Stand-alone MS tracks [95] are reconstructed in the pseudorapidity region $|\eta| \geq 0.1$ and formed by requiring at least two matched segments in the MS, and are fit with a primary vertex constraint. Candidates with pseudorapidity in the range $1.0 \leq |\eta| \leq 1.1$ are rejected to avoid the transition region of the MS between barrel and endcap. Moreover, only stand-alone MS tracks in the pseudorapidity interval $|\eta| < 2.4$, corresponding to the ID coverage, are selected to allow an isolation variable based on ID tracks to be computed. Stand-alone MS tracks are required to not match any prompt muon candidate, in order to discard muons coming from the main interaction vertex.

A γ_{d} decaying into a displaced electron or quark pair leads to energy deposits in the calorimeters reconstructed as a single jet with low EM fraction (EMF), defined as the ratio of the energy deposited in the EM calorimeter to the total jet energy. Jets with EMF below 0.4 are referred to as calorimeter dark-photon jet caloDPJ. MC simulations show that DPJs containing two dark photons both decaying into an electron or quark pair are reconstructed as a single jet. Low-EM-fraction jets are reconstructed and calibrated with the same algorithms as described previously. They are, however, only considered if they have $p_{\mathrm{T}} > 20\,\mathrm{GeV}$ and lie within $|\eta| < 2.5$. Furthermore, to retain high efficiency for the targeted signals, they are required to satisfy quality criteria looser than those in the main jet selection and no JVT selection is applied. To avoid selecting events where most of the energy associated with a jet could have been produced by localised noise, events are rejected if the leading jet has >90% of its energy associated with a single constituent cluster or layer within the LAr calorimeter. Potential background from noise bursts [96] in the LAr calorimeter is rejected via a veto on events where the leading jet's largest energy deposit is located in the EM calorimeter endcap, where most noise bursts occur. Noise-induced jets in the hadron calorimeters are removed by imposing the *BadLoose* cleaning selection, described in Ref. [88], without the cuts on the

fraction of jet energy deposited within the electromagnetic calorimeter and the jet charged-fraction. These cleaning requirements reject approximately 0.8% of low-EM-fraction jets in the signal samples used in this analysis. Finally, the time t_{caloDPJ} associated with a caloDPJ, measured as the energy-weighted average of the timing for each calorimeter cell related to the jet and corrected by the corresponding time-of-flight from the interaction point, is required to fall within a window of 4 ns around zero. CaloDPJs from cosmic-ray muons and beam-induced backgrounds (BIB) would have a different jet-timing distribution than collision products.

Dedicated algorithms for the identification of DPJs have been developed to target γ_{d} decays into μDPJs or caloDPJs. These algorithms are described in Sections 4.1 and 4.2 respectively.

4.1 Muonic dark-photon jets

Muonic dark-photon jets are reconstructed using the Cambridge–Aachen clustering algorithm [97] that combines all the selected stand-alone MS tracks lying within a cone of fixed size in (η, ϕ) space. The algorithm starts from the highest-p_{T} stand-alone MS track and searches for additional stand-alone MS tracks within a $\Delta R = 0.4$ cone around the initial track's momentum vector. If a second stand-alone MS track is found in the cone, the axis of the cone is rotated to the vector sum of the momenta of the two tracks, and the search is repeated until no additional tracks are found in the cone. The μDPJs are required to have at least two MS tracks and are discarded if a jet is found within $\Delta R = 0.4$ of a μDPJ, to ensure orthogonality between reconstructed DPJ types.

Cosmic-ray muons that cross the detector in time coincidence with a pp interaction constitute the main source of background to the μDPJ. The cosmic dataset is used to study this background and to train a dense neural network (DNN), referred to as the cosmic-ray tagger, to discriminate signal μDPJs from the μDPJ candidates that originate from the cosmic-ray background. For optimal training, a balanced mixture of all available MC signal samples is used. The DNN is implemented using Keras with the Tensorflow backend [98] and it is trained to classify each stand-alone MS track constituting a μDPJ using the following quantities: the longitudinal impact parameter z_0, the track angular direction (in η and ϕ), and the timing measurements from the MS. The time measurements in different stations of the MS, when available, allow the muon's direction of flight to be identified. A parametric training method is used to only consider the timing measurements when they are available. The neural network has three dense hidden layers, with 32, 64 and 128 neurons respectively. An output layer with a sigmoidal activation function returns a binary classification score between 0 and 1, which can be interpreted as the probability for a μDPJ constituent track to originate from a γ_{d} decay, and example distributions are shown in Figure 2. The figure also illustrates the small dependency on the specific choice of signal model. A μDPJ is accepted if all its stand-alone MS track constituents have a cosmic-ray tagger output score > 0.5. This selection was optimised to retain a high signal efficiency: signal μDPJs are selected with an efficiency above 95% for transverse decay lengths L_{xy} up to 5 m and for γ_{d} p_{T} larger than 20 GeV and with a background rejection of 90%.

The μDPJ reconstruction efficiency is shown in Figure 3, for μDPJ objects that satisfy the cosmic-ray tagger selection, as a function of the L_{xy} and transverse momentum of the dark photon in a few benchmark signal scenarios. A drop in efficiency is expected for γ_{d} decays which occur after the middle layer of the MS (6 m radius in the barrel region), where muons can no longer be reconstructed.

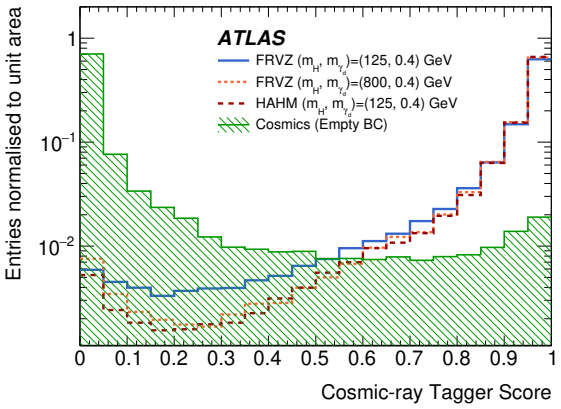

Figure 2: The distribution of the cosmic-ray tagger output score is shown for a few signal scenarios (lines) and for data from the cosmic dataset (shaded area).

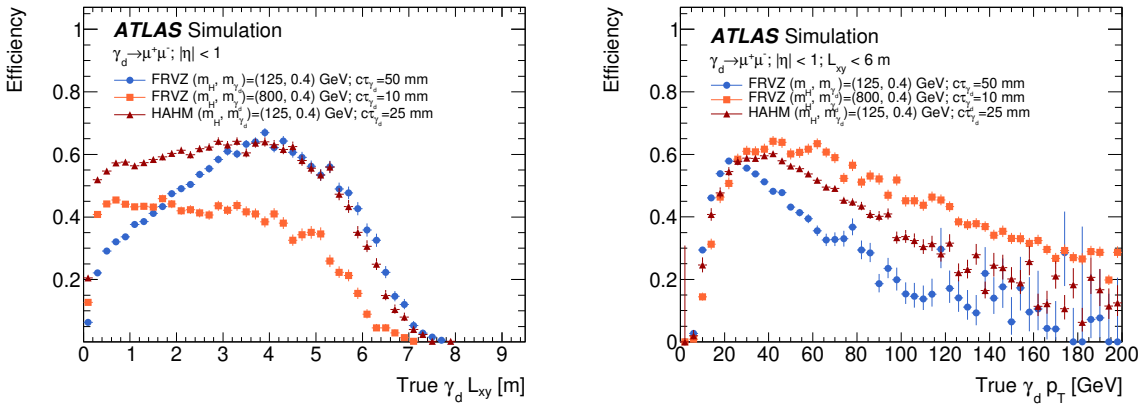

(a) (b)

Figure 3: The reconstruction efficiency for μDPJ objects satisfying the cosmic-ray tagger selection produced in the decay of a γ_{d} into a muon pair. Figure (a) shows the reconstruction efficiency for γ_{d} with $0 < |\eta| < 1$ as a function of the transverse decay length L_{xy}. Figure (b) shows the reconstruction efficiency for γ_{d} with $0 < |\eta| < 1$ as a function of the γ_{d} transverse momentum in events where the γ_{d} L_{xy} is below 6 m.

4.2 Calorimeter dark-photon jets

All the low-EM-fraction jets satisfying the selection described in Section 4 are considered as calorimeter dark-photon-jet candidates. Candidates in the transition region between the barrel calorimeters and the endcap cryostat are removed by requiring the fraction of energy in the Tile Gap scintillators to be less than 10% of the total jet energy.

The main source of background for caloDPJs is jet production. In order to reduce this background, a dedicated discriminator (QCD tagger), based on a convolutional neural network implemented using Keras with the Tensorflow backend, is used to assign a score to each caloDPJ in the event. The training of the neural network is based on simulated events and exploits caloDPJs reconstructed in signal and multi-jet MC events. The QCD tagger inputs are three-dimensional representations of energy deposits associated with the

jet. The energy deposits are defined by collections of calorimeter cell clusters used in jet reconstruction [82]. Each collection has (η, ϕ) coordinates and holds information about the total amount of energy deposited in each of the calorimeter samplings.

The (η, ϕ) space around the jet axis is divided into a 15×15 grid, centred on the jet axis and corresponding to an $\eta \times \phi = 0.9 \times 0.9$ area, so that each cell cluster within this 2D grid corresponds to a 0.06×0.06 portion of the (η, ϕ) space. A third axis is added to this grid, to take into account the EM and HCAL calorimeters' samplings as an additional coordinate. The resulting 3D grids are composed of cell clusters which contain the total energy released at the corresponding (η, ϕ) coordinates and calorimeter sampling. In order to exploit the full calorimeter volume, three 3D grids are produced: one accounting for the barrel samplings, one for the tile calorimeter's extended barrel and one for the endcap. These are then used as input to a convolutional neural network. The output layer of the neural network has a sigmoidal activation function resulting in a binary classification in the [0, 1] range, as shown in Figure 4(a).

CaloDPJs are defined to be candidates if they have a QCD tagger score larger than 0.5. This selection was optimised to retain a high signal efficiency and corresponds to a background rejection of approximately 94%. The QCD tagger has a signal efficiency above 95% for L_{xy} above 2.5 m, which decreases to about 60% for γ_d decaying within the ID. The efficiency was also found to be independent of the γ_d p_T for a p_T larger than 20 GeV.

Muons arising from BIB and crossing the detector longitudinally, at radial distances $r > 2$ m, can deposit energy in the HCAL by radiative losses, which can be reconstructed as caloDPJs owing to the resulting low EM fraction. To reduce the residual contamination from misidentified caloDPJs from BIB, a dedicated per-jet tagger (BIB tagger) was developed. This tagger uses the same strategy as the QCD tagger, exploiting the topology of the energy deposits to classify the candidate jets.

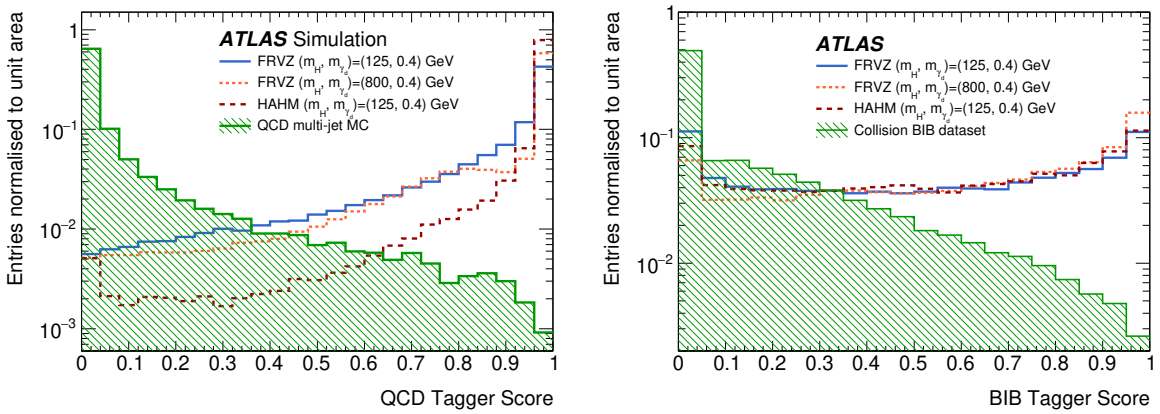

(a) (b)

Figure 4: The output score for the taggers used on calorimeter dark-photon jets. Figure (a) shows the QCD tagger score for a few signal scenarios and simulated multi-jet events. Figure (b) shows the BIB tagger score for the same signal scenarios and BIB-enriched data.

The BIB tagger shares the network architecture of the QCD tagger. To remove any possible energy dependence and rely only on geometrical information, the input tensors are preprocessed by substituting the cluster energies with a fixed value. The jet (η, ϕ) coordinates are passed as inputs to the dense neural network, in addition to the convolution layers' output. CaloDPJs from a BIB-enriched data selection and

from all available MC signal samples are used as input for the training. The BIB-enriched data selection uses a dedicated calorimeter trigger exploiting cell timing and position to select BIB events. This trigger's performance was validated on BIB events occurring during empty bunch crossings. CaloDPJs are accepted if the output score of the BIB tagger, shown in Figure 4(b), is larger than 0.2, corresponding to a BIB rejection rate of 68%. This value is chosen in order to keep the signal efficiency above 80%, irrespective of the signal scenario, for events entering the analysis selections.

The caloDPJ reconstruction efficiency is shown in Figure 5 for caloDPJ candidates that satisfy the QCD tagger selection but no BIB tagger requirement, as a function of the transverse decay length and transverse momentum, for several benchmark signal samples. A γ_{d} decaying into hadrons or electrons is reconstructed only within the HCAL volume (at radii of 2.28–4.25 m in the barrel region).

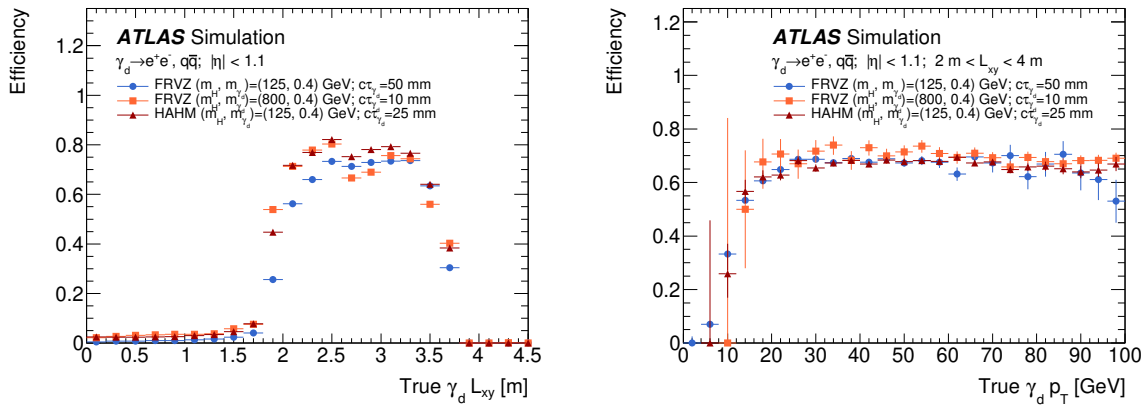

(a) (b)

Figure 5: The reconstruction efficiency for caloDPJs produced by the decay of γ_{d} into e^+e^- or $q\bar{q}$. Figure (a) shows the reconstruction efficiency for γ_{d} with $0 < |\eta| < 1.1$ as a function of the transverse decay length L_{xy}. The efficiency drop at 2.5 m corresponds to the end of the first layer of the HCAL. Figure (b) shows the reconstruction efficiency for γ_{d} with $0 < |\eta| < 1.1$ as a function of their transverse momentum in events where the γ_{d} L_{xy} is between 2 m and 4 m.

5 Event selection and background estimation

The events are classified into the two exclusive search categories, gluon–gluon fusion (ggF) and *WH* associated production, based on their charged-lepton multiplicity. The ggF category targets the Higgs boson production mode where events have no charged-lepton candidates satisfying the selections described in Section 4. The *WH* category targets Higgs boson production in association with a *W* boson and requires exactly one charged lepton. Two DPJs satisfying the selection criteria described in Section 4 are required in the selected events. If more than two DPJs are reconstructed, the one with the highest transverse momentum, called the 'leading DPJ', and the one farthest in $\Delta\phi$ from the leading one, called the 'far DPJ', are used to classify the event. Each search category further separates the events into different orthogonal search channels based on the numbers of μDPJs and caloDPJs, resulting in a total of six signal regions (SRs) that were optimised for the best discovery sensitivity.

The main sources of background for the DPJ signals are cosmic-ray muons for the μDPJs and jet production for both the caloDPJs and μDPJs. Cosmic-ray muon background for the μDPJs is strongly reduced after

the event selection, and the main residual background is found to consist of hadronic or electromagnetic showers which reach the MS after not being fully contained in the calorimeter (punch-through jets) and originate from multi-jet events. A subdominant background for both DPJ types is BIB. All background contributions are estimated from data. For the different decay modes considered, dedicated sets of the following discriminating variables are used to separate the BSM signal from the backgrounds or in the definition of regions used to aid the estimation of the background contributions:

- m_{jj}: the invariant mass of the two leading jets.
- $|\Delta t_{\mathrm{caloDPJs}}|$: the absolute time difference between a pair of caloDPJs. This quantity is useful for further rejecting contributions from cosmic-ray muons and BIB, as these caloDPJ candidates do not originate from a single interaction vertex.
- JVT: the JVT score of a caloDPJ can be used to reject candidates that are likely to originate from the primary proton–proton interaction vertex.
- $\Delta\phi_{\mathrm{DPJ}}$: the azimuthal angle between the leading DPJ and far DPJ. Signal events are expected to contain anti-aligned DPJs.
- $\sum_{\Delta R=0.5} p_{\mathrm{T}}$: the scalar sum of the transverse momenta of all tracks within a $\Delta R = 0.5$ cone around the direction of the DPJ momentum vector. Displaced DPJs are expected to have very little nearby track activity in the ID.
- $\max(\sum p_{\mathrm{T}})$: the largest of the $\sum_{\Delta R=0.5} p_{\mathrm{T}}$ values for the two DPJs in an event.
- $\prod$ QCD tagger: the product of the QCD tagger scores of the two DPJs, or the single QCD tagger score when only one caloDPJ is available.
- m_{T}: the event transverse mass, computed as $m_{\mathrm{T}} = \sqrt{2p_{\mathrm{T}}^{\ell} E_{\mathrm{T}}^{\mathrm{miss}}(1 - \cos\Delta\phi)}$ where $\Delta\phi$ is the azimuthal angle between the missing transverse momentum vector and the lepton, is exploited to reduce possible background contributions from multi-jet processes with a misidentified or non-prompt lepton.
- caloDPJ width: the p_{T}-weighted sum of the ΔR between each energy cluster of the jet and the jet axis. Jets from DPJs are expected to be narrower, on average, than ordinary jets since they are produced just before or inside the calorimeters.
- $\min(\Delta\phi)$: smallest azimuthal angular separation between a selected DPJ and the $\mathbf{p}_{\mathrm{T}}^{\mathrm{miss}}$ vector.
- min(QCD tagger): the minimum QCD tagger score, computed for up to two caloDPJs in an event.

The detailed selection requirements, together with the dedicated methods for the estimation of the residual background contributions, are described in Section 5.1 for the ggF selection and in Section 5.2 for the *WH* selection.

5.1 Gluon–gluon fusion selection

In this selection, events are accepted if they satisfy one or more of three dedicated triggers targeting displaced objects. The trigger strategy is analogous to that described in Ref. [14]. It comprises two MS-based triggers and one calorimeter-based trigger.

The first MS-based trigger, referred to as tri-muon MS-only [57], accepts events with at least three muons with $p_{\mathrm{T}} \geq 6$ GeV reconstructed using only MS information. The second MS-based trigger, referred to as

muon narrow-scan [99], requires a muon candidate from the L1 trigger with $p_{\mathrm{T}} \geq 20$ GeV to be confirmed by the HLT using only MS information. At the HLT a 'scan' is then performed in a cone of $\Delta R = 0.5$ around this muon, looking for a second muon reconstructed using only MS information. The p_{T} requirement on the second muon was increased from 6 GeV to 15 GeV during the course of the 2015–2016 data taking and kept constant afterwards. Both muons were required to be not matched to any track in the ID, and track isolation was required for the leading muon. During the 2017–2018 data taking, the narrow-scan trigger was extended to take advantage of the L1 topological trigger [100] by requiring partially matched topological items. The leading L1 muon candidate was then combined with an HLT object: either an unmatched muon, a jet, or transverse momentum imbalance. The last two were added to target events with one μDPJ and one caloDPJ. The narrow-scan triggers have constant efficiencies of 75% and 40% for the 2015–2016 and 2017–2018 versions, respectively, when considering events with γ_{d} decays into muon pairs with $|\eta| < 1.0$ and L_{xy} below 6 m.

A L1 calorimeter trigger called the CalRatio trigger [99] is designed to select narrow jets produced in the hadronic calorimeter. During 2015–2016, the CalRatio L1 trigger selected narrow jets with transverse energy $E_{\mathrm{T}} > 60$ GeV in a 0.2×0.2 ($\Delta\eta \times \Delta\phi$) region of the EM and HCAL. During 2017–2018 data taking, the CalRatio trigger instead used a L1 topological trigger [100] to select jets in the HCAL that have $E_{\mathrm{T}} > 30$ GeV and are isolated from energy deposits in the EM calorimeter with $E_{\mathrm{T}} > 3$ GeV within $\Delta R = 0.2$ around the most energetic HCAL energy deposit. At the HLT, jets from both of these L1 selections were required to have $E_{\mathrm{T}} \geq 30$ GeV, $|\eta| < 2.4$ and EM fraction < 0.06. These jets were also required to have no tracks with $p_{\mathrm{T}} \geq 2$ GeV within $\Delta R = 0.2$ of the jet axis, and to satisfy BIB-suppression requirements on calorimeter cell timing and position. The CalRatio triggers used in 2015–2016 and 2017–2018 are found to have constant efficiencies of approximately 5% and 20%, respectively, for FRVZ signal events where the γ_{d} is produced in the decay of a 125 GeV Higgs boson and decays into e^+e^- or $q\bar{q}$ within $|\eta| < 1.0$. These efficiencies rise to 25% and 30%, on average, for signal events in HAHM models, or to 55% and 45%, on average, when assuming γ_{d} production via an 800 GeV scalar mediator.

Events where the two leading jets have an invariant mass $m_{\mathrm{jj}} > 1$ TeV and $E_{\mathrm{T}}^{\mathrm{miss}} > 225$ GeV are removed to allow for a statistically independent study of vector-boson fusion (VBF) production modes in the future.

The events satisfying the requirements listed above are further separated into orthogonal search channels based on the DPJ types. Events with pairs of μDPJs (caloDPJs) are targeted by $\mathrm{SR}_{2\mu}^{\mathrm{ggF}}$ ($\mathrm{SR}_{2\mathrm{c}}^{\mathrm{ggF}}$), while events with one DPJ of each kind are targeted by $\mathrm{SR}_{\mathrm{c}+\mu}^{\mathrm{ggF}}$. Each of these SRs includes additional selection requirements, as summarised in Table 1 together with the triggers employed. The impact of beam-induced background is suppressed by requiring caloDPJ candidates to pass the BIB tagger selection and, only in the $\mathrm{SR}_{2\mathrm{c}}^{\mathrm{ggF}}$ where two caloDPJs are reconstructed, to have a time difference $|\Delta t_{\mathrm{caloDPJs}}|$ smaller than 2.5 ns. In $\mathrm{SR}_{2\mathrm{c}}^{\mathrm{ggF}}$ and $\mathrm{SR}_{\mathrm{c}+\mu}^{\mathrm{ggF}}$, the leading and far DPJs are further required to have an azimuthal angular difference $\Delta\phi_{\mathrm{DPJ}}$ larger than 0.5. Multi-jet background events are rejected by requiring the DPJs to satisfy ID isolation criteria. DPJ candidates are required to have a $\sum_{\Delta R=0.5} p_{\mathrm{T}}$ below 4.5 GeV.

The main sources of background after the SR selections are punch-through jets from rare multi-jet events for $\mathrm{SR}_{2\mu}^{\mathrm{ggF}}$ and multi-jet production for $\mathrm{SR}_{2\mathrm{c}}^{\mathrm{ggF}}$ and $\mathrm{SR}_{\mathrm{c}+\mu}^{\mathrm{ggF}}$. The second leading background for all SRs is the cosmic-ray muon background.

In order to estimate the background contribution to each SR, a data-driven 'ABCD' method is used. This method relies on the assumption that the distribution of background events can be factorised in the plane of two uncorrelated variables so that it is subdivided into four regions: A, B, C, and D. The number of background events in the SR can be evaluated as $N_{\mathrm{A}} = N_{\mathrm{D}} \times N_{\mathrm{B}}/N_{\mathrm{C}}$. Any possible signal leakage outside

Table 1: Definition of the SRs used in the ggF selection. All SRs require at least two DPJs, but only the leading and the far DPJs are considered for the event classification. Dashes indicate cases where a requirement is not applied.

Requirement / Region	$SR_{2\mu}^{ggF}$	SR_{2c}^{ggF}	$SR_{c+\mu}^{ggF}$
Number of μDPJs	2	0	1
Number of caloDPJs	0	2	1
Tri-muon MS-only trigger	yes	-	-
Muon narrow-scan trigger	yes	-	yes
CalRatio trigger	-	yes	-
$\lvert\Delta t_{\text{caloDPJs}}\rvert$ [ns]	-	< 2.5	-
caloDPJ JVT	-	< 0.4	-
$\Delta\phi_{\text{DPJ}}$	$> \pi/5$	$> \pi/5$	$> \pi/5$
BIB tagger score	-	> 0.2	> 0.2
$\max(\sum p_{\text{T}})$ [GeV]	< 4.5	< 4.5	< 4.5
$\prod$ QCD tagger	-	> 0.95	> 0.9

the SR region is accounted for by using a modified ABCD method that simultaneously fits the signal and background events, taking into account potential signal contamination in the ABCD estimate.

The planes used in the estimation of the backgrounds for the three ggF SRs are formed by $\max(\sum p_{\text{T}})$ and either $\Delta\phi_{\text{DPJ}}$ in $SR_{2\mu}^{ggF}$, or $\prod$ QCD tagger in SR_{2c}^{ggF} and $SR_{c+\mu}^{ggF}$. The definition of the three sets of ABCD control regions are given in Table 2. In the ABCD convention, region A is the SR and regions B, C and D are respectively the control regions CRB, CRC and CRD.

The cosmic-ray muon background contribution is estimated first, using the cosmic dataset. The ratio of the number of filled bunch crossings to the number of empty bunch crossings is used to scale the number of events in the cosmic dataset to that in the pp collision data. The value of this correction depends on the trigger used in the SR selection and ranges from a minimum of 2.2 for the CalRatio trigger in 2015–2016 to a maximum of 3.9 for the tri-muon MS-only trigger in 2018. Only three regions were found to have a non-negligible cosmic-ray muon background contribution: 7 ± 5 events in $SR_{2\mu}^{ggF}$, 7 ± 4 events in SR_{2c}^{ggF} and 14 ± 7 events in CRD_{2c}^{ggF}. Since the events forming the cosmic dataset are collected in empty bunch crossings, there is no significant activity in the ID, which implies that the $\sum p_{\text{T}}$ is 0 for all reconstructed DPJs. For this reason, events populate only the SRs and CRD. These estimated cosmic-ray muon backgrounds are subtracted from the observed data in the main dataset before performing the ABCD procedure.

Events with BIB energy deposits are very likely to have two caloDPJs which can contribute to the background. The possible contribution from misidentified caloDPJs was studied using the BIB-enriched dataset. This selection is thus orthogonal to the signal regions. The efficiency of the SR and CR selection requirements when applied to BIB-enriched events was found to be less than $2.3 \cdot 10^{-4}$, reducing the BIB contamination to a negligible contribution. The BIB background is hence neglected.

Figure 6 shows the distribution of data events in the ABCD plane for the three search channels, together

Table 2: Definition of the control regions used in the ggF background estimation. All control regions require at least two DPJs, but only the leading DPJ and the far DPJ are considered for the event classification. All CR requirements are the same as for the respective SR, with the exception of the selections reported in this table.

Requirement / Region	$\mathrm{CRB}_{2\mu}^{\mathrm{ggF}}$	$\mathrm{CRC}_{2\mu}^{\mathrm{ggF}}$	$\mathrm{CRD}_{2\mu}^{\mathrm{ggF}}$
$\Delta\phi_{\mathrm{DPJ}}$	$> \pi/5$	$(0.1, \pi/5]$	$(0.1, \pi/5]$
$\max(\sum p_{\mathrm{T}})$ [GeV]	$[4.5, 20)$	$[4.5, 20)$	< 4.5
Requirement / Region	$\mathrm{CRB}_{2\mathrm{c}}^{\mathrm{ggF}}$	$\mathrm{CRC}_{2\mathrm{c}}^{\mathrm{ggF}}$	$\mathrm{CRD}_{2\mathrm{c}}^{\mathrm{ggF}}$
$\prod$ QCD tagger	> 0.95	$(0.8, 0.95]$	$(0.8, 0.95]$
$\max(\sum p_{\mathrm{T}})$ [GeV]	$[4.5, 20)$	$[4.5, 20)$	< 4.5
Requirement / Region	$\mathrm{CRB}_{\mathrm{c}+\mu}^{\mathrm{ggF}}$	$\mathrm{CRC}_{\mathrm{c}+\mu}^{\mathrm{ggF}}$	$\mathrm{CRD}_{\mathrm{c}+\mu}^{\mathrm{ggF}}$
$\prod$ QCD tagger	> 0.9	$(0.75, 0.9]$	$(0.75, 0.9]$
$\max(\sum p_{\mathrm{T}})$ [GeV]	$[4.5, 20)$	$[4.5, 20)$	< 4.5

with the expected distribution for a benchmark FRVZ model assuming a 125 GeV Higgs boson and a decay branching fraction to the dark sector of 10%. The acceptance times efficiency for the FRVZ signal processes after applying all selection criteria is 0.74%, 0.02% and 0.15%, in the case of a γ_{d} mass of 400 MeV and a generated $c\tau$ of 50 mm, for the signal regions $\mathrm{SR}_{2\mu}^{\mathrm{ggF}}$, $\mathrm{SR}_{2\mathrm{c}}^{\mathrm{ggF}}$ and $\mathrm{SR}_{\mathrm{c}+\mu}^{\mathrm{ggF}}$ respectively.

The background estimation procedure was validated by applying the ABCD method in subregions constructed in combinations of the regions CRB, CRC and CRD, for varying choices of the subregion boundaries. For each validation test, a new set of $(\mathrm{ABCD})'$ test regions was defined within the union of either CRB and CRC or CRC and CRD. The test region boundaries were varied in discrete steps after dividing the allowed range into ten equal-size intervals. The validation was performed for each of the $\mathrm{SR}_{2\mu}^{\mathrm{ggF}}$, $\mathrm{SR}_{2\mathrm{c}}^{\mathrm{ggF}}$ and $\mathrm{SR}_{\mathrm{c}+\mu}^{\mathrm{ggF}}$ selections. The expected background yields in the resulting test SRs range between 15 and 800 events. An additional validation of the method was performed by checking the closure on orthogonal selections, which were obtained either by inverting the cosmic-ray tagger cut or by selecting different ranges of QCD tagger score. These selections were chosen in order to have negligible signal contributions. In all the channels, the observed yields were found to agree within one standard deviation with the expected yields. The Pearson linear correlation coefficient between the two variables defining the ABCD plane in all subregions and in the validation regions was found to be less than 3%. The signal leakage in regions CRB, CRC and CRD, was found to be less than 10% of the total signal in the ABCD selection for all signal scenarios considered in the analysis.

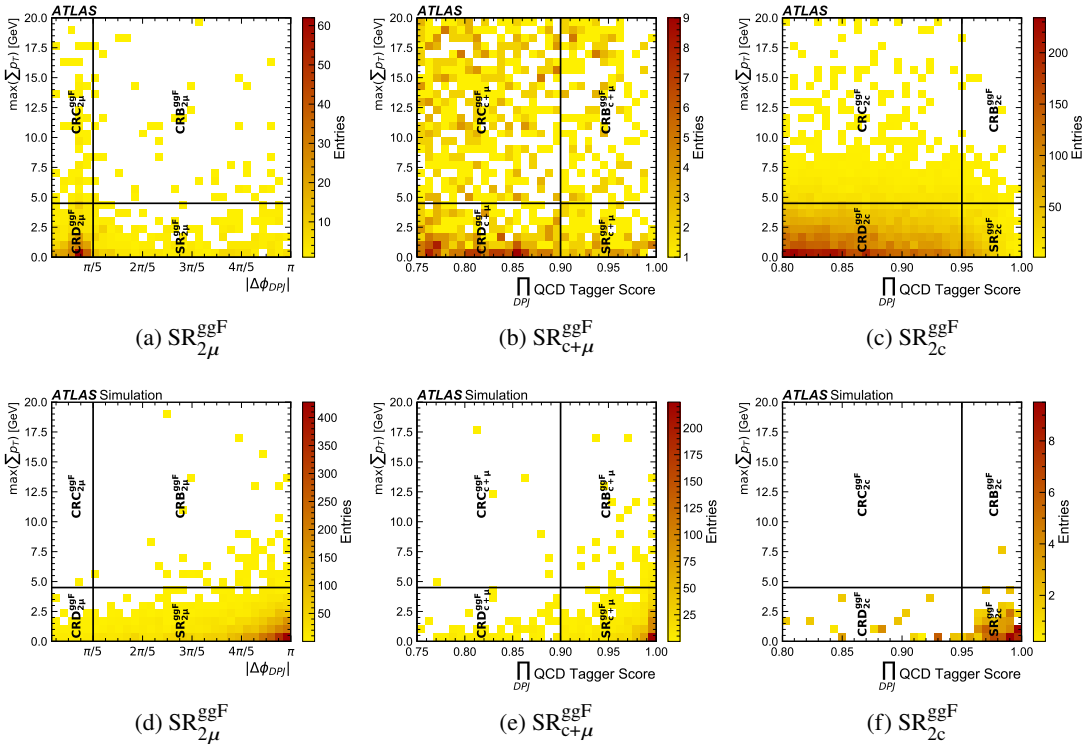

(a) $\mathrm{SR}^{\mathrm{ggF}}_{2\mu}$ (b) $\mathrm{SR}^{\mathrm{ggF}}_{\mathrm{c}+\mu}$ (c) $\mathrm{SR}^{\mathrm{ggF}}_{2\mathrm{c}}$

(d) $\mathrm{SR}^{\mathrm{ggF}}_{2\mu}$ (e) $\mathrm{SR}^{\mathrm{ggF}}_{\mathrm{c}+\mu}$ (f) $\mathrm{SR}^{\mathrm{ggF}}_{2\mathrm{c}}$

Figure 6: The per-event distributions in the ABCD planes defined for the ggF search channels. Figures (a, b, c) show data events, while Figures (d, e, f) show simulated signal events. FRVZ signal samples assuming a 125 GeV Higgs boson with a decay branching fraction of 10% to the dark sector and a γ_{d} mass of 400 MeV are shown.

5.2 *WH* associated production selection

In the *WH* selection, candidate events are required to pass single-electron or single-muon triggers. The offline requirements on the p_{T}, identification and isolation of the lepton are tighter than those applied online, so as to be on the trigger efficiency plateau [54].

The selection requires one electron or muon with $p_{\mathrm{T}} \geq 27$ GeV, $E_{\mathrm{T}}^{\mathrm{miss}} \geq 30$ GeV, $m_{\mathrm{T}} \geq 40$ GeV, and no additional lepton with $p_{\mathrm{T}} \geq 10$ GeV. Events where the two leading jets have an invariant mass $m_{\mathrm{jj}} \geq 1$ TeV are removed to allow for a future statistically independent study of VBF production modes. Contributions from single-top and $t\bar{t}$ processes are reduced by requiring three or fewer jets with $p_{\mathrm{T}} \geq 30$ GeV and no b-tagged jets in each event. After these selections the background is dominated by W+jets events.

Events are then separated into orthogonal search channels based on the numbers of μDPJs and caloDPJs. Events with exactly one caloDPJ are targeted by $\mathrm{SR}^{WH}_{\mathrm{c}}$, and events with two or more caloDPJs by $\mathrm{SR}^{WH}_{2\mathrm{c}}$. The mixed channel with one DPJ of each type is targeted by $\mathrm{SR}^{WH}_{\mathrm{c}+\mu}$. Channels with only μDPJs are not considered for the *WH* selection as the constraints they provide are not competitive with those from other signal production modes. The SR requirements are summarised in Table 3. In all SRs, caloDPJ candidates are required to have a JVT score below 0.6 to suppress jets originating from the interaction point. Events belonging to $\mathrm{SR}^{WH}_{\mathrm{c}}$, where one γ_{d} is reconstructed, are required to have $m_{\mathrm{T}} \geq 120$ GeV and a caloDPJ with $p_{\mathrm{T}} \geq 30$ GeV to further reduce the initially overwhelming W+jets background. In this SR, the second γ_{d} is expected to decay outside the detector volume and yield a higher $E_{\mathrm{T}}^{\mathrm{miss}}$. CaloDPJ candidates are

required to have a width $w \leq 0.08$ in $\mathrm{SR}_{\mathrm{c}}^{WH}$ and $w \leq 0.1$ in $\mathrm{SR}_{\mathrm{c+}\mu}^{WH}$. In $\mathrm{SR}_{\mathrm{2c}}^{WH}$ the leading (far) caloDPJ candidate is required to have $w \leq 0.1$ (0.15). These selections are optimised to reject hadronic jets and maximise the discovery significance.

Table 3: Definition of the signal regions used in the *WH* selection. In signal regions requiring at least two DPJs, only the leading DPJ and the far DPJ are considered for the event classification. Each DPJ SR is exclusive in the number of DPJs in the event. Dashes indicate cases where a requirement is not applied.

Requirement / Region	$\mathrm{SR}_{\mathrm{c}}^{WH}$	$\mathrm{SR}_{\mathrm{2c}}^{WH}$	$\mathrm{SR}_{\mathrm{c+}\mu}^{WH}$
Number of μDPJs	0	0	1
Number of caloDPJs	1	2	1
Single-lepton trigger (μ, e)	yes	yes	yes
m_{T} [GeV]	> 120	-	-
$\lvert t_{\mathrm{caloDPJ}} \rvert$ [ns]	< 4	< 4	< 4
Leading (far) caloDPJ width	< 0.08	< 0.10 (0.15)	< 0.1
caloDPJ p_{T} [GeV]	> 30	-	-
JVT	< 0.6	< 0.6	< 0.6
$\min(\Delta\phi)$	$< 3\pi/5$	$< 3\pi/10$	$< 7\pi/20$
min(QCD tagger)	> 0.99	> 0.91	> 0.9

After the selection the main background is due to W+jets events where rare QCD phenomena give rise to in-flight decays and punch-through jets that mimic signal DPJs. The residual W+jets background in the signal region is estimated with a data-driven ABCD method, the same as used for the ggF selection and explained in detail in Section 5.1. The non-collision background from cosmic-ray muons and BIB was found to be negligible for this selection.

The ABCD planes used in the estimation of the backgrounds for the three *WH* SRs are based on $\min(\Delta\phi)$ and min(QCD tagger). These variables provide good discrimination between signal and background, and are highly uncorrelated in W+jets events. The definitions of the three sets of ABCD regions are given in Table 4.

All the SRs lie at high QCD tagger score and small azimuthal angular separation between the $\mathbf{p}_{\mathrm{T}}^{\mathrm{miss}}$ and the nearest DPJ, where most of the signal events are expected.

The background estimation procedure was validated by applying the ABCD method in subregions constructed in combinations of the regions CRB, CRC and CRD, for various choices of the subregion boundaries, as done for the ggF selection. The expected background yields in the resulting test SRs range between 80 and 1550 events. Excellent agreement, within one standard deviation, between data and the predicted yields was observed in most regions, with discrepancies of up to two standard deviations appearing in the validation of $\mathrm{SR}_{\mathrm{c}}^{WH}$ for values of min(QCD tagger) close to 0.9. An additional validation of the method was performed by checking the closure of the ABCD procedure on orthogonal selections, which were obtained by selecting different ranges of QCD tagger score. The validation ranges extend to a minimum of 0.6. In all the channels, the observed yields were found to agree within one standard deviation

Table 4: Definition of the control regions used in the *WH* background estimation. The requirements for all regions are the same as those for the respective SRs, except for the selections reported in this table.

Requirement / Region	$\mathrm{CRB}_{\mathrm{c}}^{WH}$	$\mathrm{CRC}_{\mathrm{c}}^{WH}$	$\mathrm{CRD}_{\mathrm{c}}^{WH}$
$\min(\Delta\phi)$	$< 3\pi/5$	$> 3\pi/5$	$> 3\pi/5$
min(QCD tagger)	$[0.9, 0.99)$	$[0.9, 0.99)$	> 0.99
Requirement / Region	$\mathrm{CRB}_{\mathrm{2c}}^{WH}$	$\mathrm{CRC}_{\mathrm{2c}}^{WH}$	$\mathrm{CRD}_{\mathrm{2c}}^{WH}$
$\min(\Delta\phi)$	$< 3\pi/10$	$> 3\pi/10$	$> 3\pi/10$
min(QCD tagger)	$[0.8, 0.91)$	$[0.8, 0.91)$	> 0.91
Requirement / Region	$\mathrm{CRB}_{\mathrm{c}+\mu}^{WH}$	$\mathrm{CRC}_{\mathrm{c}+\mu}^{WH}$	$\mathrm{CRD}_{\mathrm{c}+\mu}^{WH}$
$\min(\Delta\phi)$	$< 7\pi/20$	$> 7\pi/20$	$> 7\pi/20$
min(QCD tagger)	$[0.8, 0.9)$	$[0.8, 0.9)$	> 0.9

with the expected yields. The Pearson linear correlation coefficient between the two variables defining the ABCD plane in all subregions and in the validation regions was found to be less than 2%.

Figure 7 shows the distribution of data events in the ABCD plane for the three search channels, together with the expected distribution for a benchmark FRVZ model assuming a 125 GeV Higgs boson. The acceptance times efficiency for the FRVZ signal processes after applying all selection criteria is 0.12% in the case of a γ_{d} mass of 400 MeV and $c\tau$ of 50 mm in $\mathrm{SR}_{\mathrm{c}+\mu}^{WH}$, and 0.05% and 0.26% in $\mathrm{SR}_{\mathrm{2c}}^{WH}$ and $\mathrm{SR}_{\mathrm{c}}^{WH}$, respectively, in the case of a γ_{d} mass of 100 MeV and $c\tau$ of 15 mm. The signal leakage in the CRs can be as high as 25% for CRB, and up to 15% for CRD and CRC. However, the stability of the fit is not affected by the potential signal leakage because the expected signal yields are negligible in comparison with the SM background in those regions.

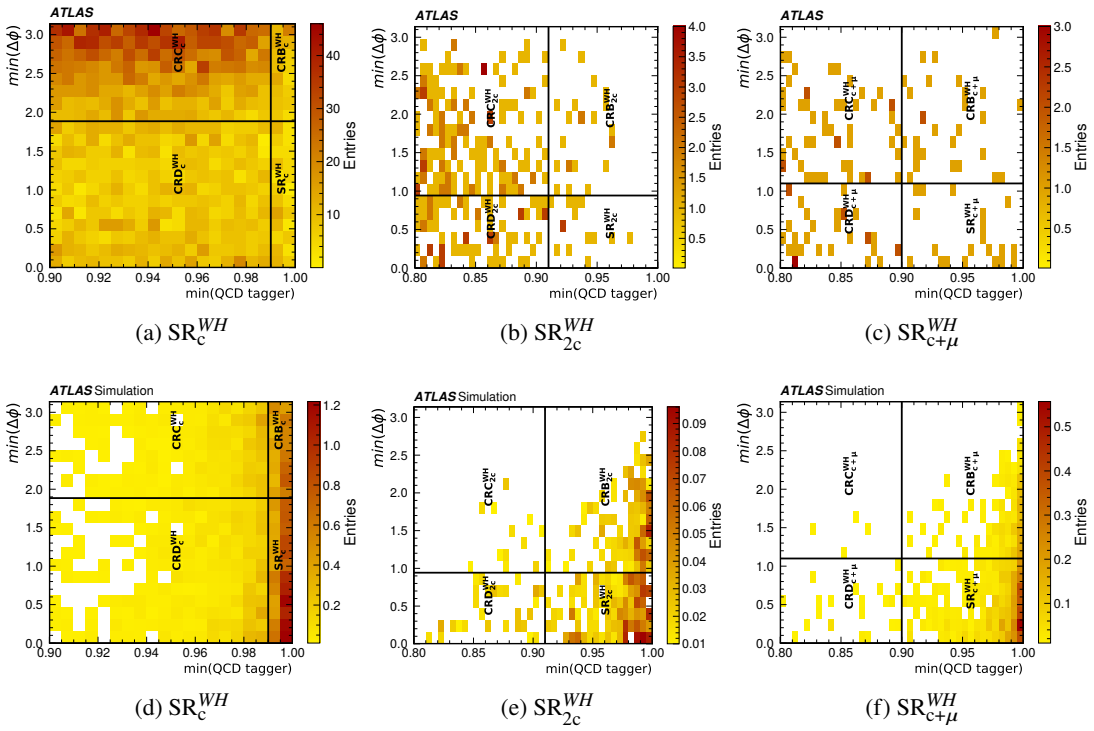

(a) $\mathrm{SR_c^{WH}}$ (b) $\mathrm{SR_{2c}^{WH}}$ (c) $\mathrm{SR_{c+\mu}^{WH}}$

(d) $\mathrm{SR_c^{WH}}$ (e) $\mathrm{SR_{2c}^{WH}}$ (f) $\mathrm{SR_{c+\mu}^{WH}}$

Figure 7: The per-event min($\Delta\phi$) vs min(QCD tagger) distributions for the *WH* search channels. Figures (a, b, c) show data, while Figures (d, e, f) show simulated signal events. FRVZ signal samples with a 125 GeV Higgs boson and a γ_d mass of 100 MeV are shown for $\mathrm{SR_c^{WH}}$ and $\mathrm{SR_{2c}^{WH}}$, while a γ_d mass of 400 MeV is shown for $\mathrm{SR_{c+\mu}^{WH}}$.

6 Systematic uncertainties

The overall uncertainty in the SR yields is dominated by the statistical uncertainty. Nevertheless, potential sources of experimental uncertainty are considered for the background estimates and the simulated signal yields.

The statistical uncertainties of the observed yields in regions CRB, CRC, and CRD are propagated to the background expectation obtained from the ABCD method. An additional uncertainty is assigned to account for the size of the cosmic dataset and scaled by the ratio of the number of empty bunch crossings to the number of filled bunch crossings while the triggers were active. This uncertainty is estimated to be as large as 80% of the expected cosmic-ray muon background, but has no impact on the final results because of the limited contribution from this specific background.

Experimental uncertainties in the reconstruction and simulation of the signal events are considered. For jets, these include jet energy resolution (JER) and jet energy scale (JES) uncertainties from the standard calibration scheme [86], which amount to up to 3% of the expected signal yields. An extra JES uncertainty is applied to take into account a possible dependence on the low-EM-fraction selection. It is estimated following the same procedure as used in the 2015–2016 dark-photon jet search [14] and is about 3%.

For muons, a systematic uncertainty in the single-γ_d reconstruction efficiency is evaluated using a tag-and-probe method applied to $J/\psi \to \mu\mu$ events in data and simulation, as $J/\psi \to \mu\mu$ decays were found to behave similarly to γ_d decays in simulated events. The J/ψ reconstruction efficiency is evaluated in both

data and simulation as a function of the opening angle ΔR between the two muons. For low ΔR values, the efficiency decreases due to the difficulty of reconstructing two tracks with small angular separation in the MS. The difference in $J/\psi \to \mu\mu$ reconstruction efficiency between simulation and data in the ΔR interval between 0 and 0.06, where the DPJ samples are concentrated, amounts to 9.6% and is taken as the uncertainty.

The systematic uncertainties in the efficiency of the two dedicated muon triggers are evaluated using a tag-and-probe method applied to $J/\psi \to \mu\mu$ events in data and simulation. The difference between the trigger efficiency in data and that in simulation is evaluated as a function of the opening angle between the two muons. The difference in the region $\Delta R < 0.05$, corresponding to the ΔR expected for signal, is taken as the uncertainty and is found to be 6% for the muon narrow-scan trigger and 5.8% for the tri-muon MS-only trigger.

The systematic uncertainty in the CalRatio trigger efficiency is taken from Ref. [101] and recomputed for each signal sample. It is estimated to be up to 4% for the heavy (800 GeV) scalar-mediator signal samples, and up to 30% for the 125 GeV Higgs signal samples.

The uncertainty associated with the MC modelling of the input variables used for the cosmic-ray tagger training is evaluated by comparing the distributions of the tagger's output scores for $Z \to \mu\mu$ events in data and MC samples. Due to the high boost of low-mass dark photons and the high p_{T} of signal muons, the muon z_0 and timing distributions are similar to those of prompt muons from $Z \to \mu\mu$ decays. Muons from Z boson decays were reconstructed using only MS information. The ratio of the two score distributions is computed and applied as a binned scale factor to the muons used for μDPJ reconstruction. The resulting relative variation of the final signal yield in the SR is taken as the systematic uncertainty. The same procedure is used for the QCD and BIB taggers, where the ratios of data to simulated distributions are computed from data and MC samples of multi-jet events after selecting signal-like events with reconstructed caloDPJs but failing the analysis trigger selections. In-depth modelling studies of jet calorimeter-cell clusters, upon which the taggers' training images are built, show no significant mis-modelling.

A pile-up modelling uncertainty is assigned to account for the difference between the predicted and measured inelastic cross-sections [102].

Finally, an uncertainty in the computed total integrated luminosity used to rescale the expected number of signal events is considered. The uncertainty in the combined 2015–2018 integrated luminosity is 1.7% [103], obtained using the LUCID-2 detector [104] for the primary luminosity measurements.

A summary of the experimental systematic uncertainties taken into account for the signal samples in this analysis is shown in Figure 8, assuming signal production via a 125 GeV Higgs boson. The average uncertainties are representative for the bulk of the signal samples, with small variations of the order of a few percent being observed as a function of the γ_{d} mass. The uncertainty related to the efficiency of the CalRatio trigger was found to have the largest variation, ranging between 15% and 26% with a linear dependence on the γ_{d} mass.

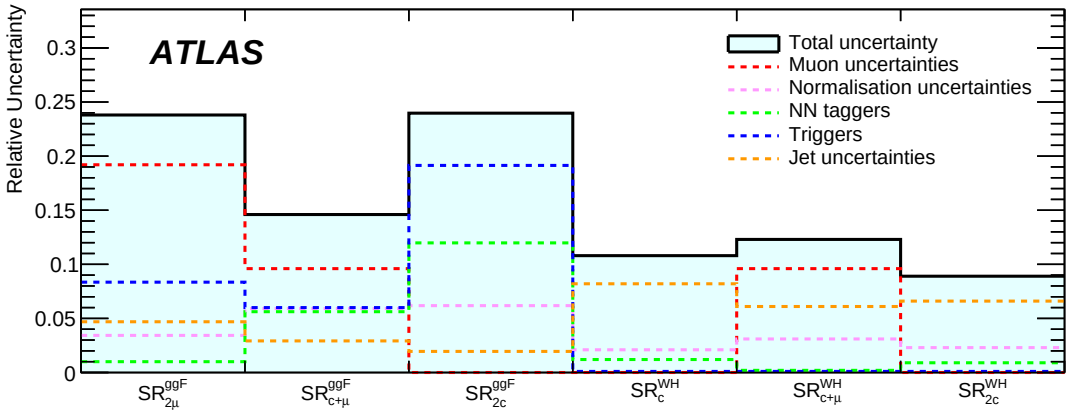

Figure 8: Comparison of the relative uncertainty in the signal yield in each SR, showing the contributions from the different sources of uncertainty. The quoted values are averaged over different γ_d masses, in scenarios assuming signal production via a 125 GeV Higgs boson. The 'Muon uncertainties' category contains all muon-related systematic uncertainties and is dominated by the uncertainty in the single-γ_d reconstruction efficiency. The 'NN taggers' category contains the three taggers adopted in the analysis and is dominated by the BIB tagger uncertainties for the hadronic channels and by the cosmic-ray tagger in the muonic channels. The 'Triggers' category contains all trigger systematic uncertainties, which are relevant only for the dedicated triggers in the ggF selection. The 'Jet uncertainties' category contains the JES, JER and low-EM-fraction JES systematic uncertainties. Some sets of systematic uncertainties apply to only a subset of the SRs.

7 Results and interpretations

The data-driven background estimate in each SR is obtained by performing a maximum-likelihood fit to the yields in the four (i.e. ABCD) regions in data. The fitted likelihood function is formed from a product of Poisson functions, one for each of the SR, CRB, CRC, and CRD regions, describing signal and background expectations. The ABCD ansatz is introduced as nuisance parameters in the background component of the expected yield in each region. The likelihood-based ABCD fit is robust against control regions with a small number of events and takes into account possible signal contamination in the control regions. All systematic uncertainties described in Section 6 are included in the fit as nuisance parameters, parameterised with Gaussian probability density functions that multiply the fit likelihood. They are assumed to be uncorrelated across regions. An alternative correlation model, where the uncertainties are assumed to be fully correlated across regions, has a negligible impact on the results. The mean value of the Gaussian probability distribution function is constrained by the nominal value of the parameter and the variance is defined by the 68% confidence interval of the systematic uncertainty associated with the parameter.

The observed and expected numbers of events in the signal regions are summarised in Table 5. The reported yields are extrapolated by the fit assuming no signal, and with unblinded data in all ABCD regions in the fit. When comparing the results with a likelihood fit using blinded data in the SR, the background yields are found to be consistent at the percent level except for $\mathrm{SR}_{2\mu}^{\mathrm{ggF}}$, where an 11% change is observed. For the ggF selection results, the estimated cosmic-ray muon yields are subtracted from each of the ABCD regions before using the ABCD method to estimate the multi-jet background yield.

The results of the search are used to set upper limits on the production cross-section times branching fraction, $\sigma \times B$, of the process $pp \to H \to 2\gamma_d + X$, with X assumed to be undetected, as a function

Table 5: Observed and expected yields in the ABCD regions. The total uncertainty in the background expectation is computed by the ABCD fit to unblinded data. In the ggF selection regions the estimated contribution from cosmic-ray muons is subtracted from each of the ABCD regions before the ABCD fit, and added back post-fit (as shown in this table).

Selection	Search channel	CRB	CRC	CRD	SR expected	SR observed
ggF	2μ	55	61	389	317 ± 47	269
	c+μ	169	471	301	108 ± 13	110
	2c	97	1113	12146	1055 ± 82	1045
WH	c	1850	3011	155	93 ± 12	103
	c+μ	30	49	31	19 ± 8	20
	2c	79	155	27	14 ± 5	15

of the γ_d mean proper decay length $c\tau$. The upper limit on the signal strength is obtained with the CL_s method [105] with the asymptotic calculator [106], considering the background and the predicted signal yields from simulation in the four ABCD regions. The validity of the asymptotic approximation is checked against a full calculation using pseudo-experiments, and the CL_s values of the two methods typically agree within 1%, and maximally within 5%. Model-dependent limits are computed for the various signal scenarios considered in the analysis. The hypothesis tests take account of the expected signal yield and its uncertainties in the CRs and SRs and are performed with a likelihood fit to the observed data.

A summary of the observed limits for scenarios assuming the production of a 125 GeV Higgs boson that can decay into hidden-sector particles, resulting in two γ_d in an FRVZ model, is shown in Figures 9 and 10 for the ggF and *WH* selections, respectively. The sensitivity of each search channel is reported in a separate subfigure. The sensitivity of the 2μ and c+μ selections to γ_d masses less than twice the muon mass is due to signal decays into a displaced electron or quark pair within the muon spectrometer volume which are reconstructed as μDPJs. For pairs of dark photons decaying into μDPJs, branching fractions larger than 1% are excluded at 95% confidence level (CL) if the dark photons have a mean proper decay length $c\tau$ between 10 mm and 250 mm and a mass between 0.4 GeV and 2 GeV. When considering dark-photon decays into pairs of caloDPJs, branching fractions larger than 10% are excluded at 95% CL for mean proper decay lengths between 2 mm and 3 mm and masses between 17 MeV and 50 MeV.

Figure 11 reports the observed limits for scenarios assuming the production of a 125 GeV Higgs boson that can decay into two γ_d in the HAHM model. The sensitivity of each search channel in the ggF selection is reported in a separate subfigure. The sensitivities in the *WH* selection are significantly lower because the CalRatio trigger is less efficient for those events. For pairs of dark photons decaying into μDPJs, branching fractions larger than 1% are excluded at 95% CL if the dark photons have a mean proper decay length $c\tau$ between 4 mm and 200 mm and a mass between 0.4 GeV and 2 GeV. When considering dark-photon decays into pairs of caloDPJs, branching fractions larger than 10% are excluded at 95% CL for mean proper decay lengths between 1.5 mm and 8 mm and masses between 17 MeV and 100 MeV.

Alternative signal scenarios were also considered in the context of FRVZ models. The sensitivity to scenarios where a pair of dark photons is produced in the decay of an 800 GeV scalar mediator is driven by the selection efficiency being higher than for the decay of the 125 GeV Higgs boson because of the harder dark-photon energy spectrum. The signal region targeting decays into one caloDPJ and one μDPJ in the ggF selection was found to be the most sensitive: branching fractions above 10% are excluded at

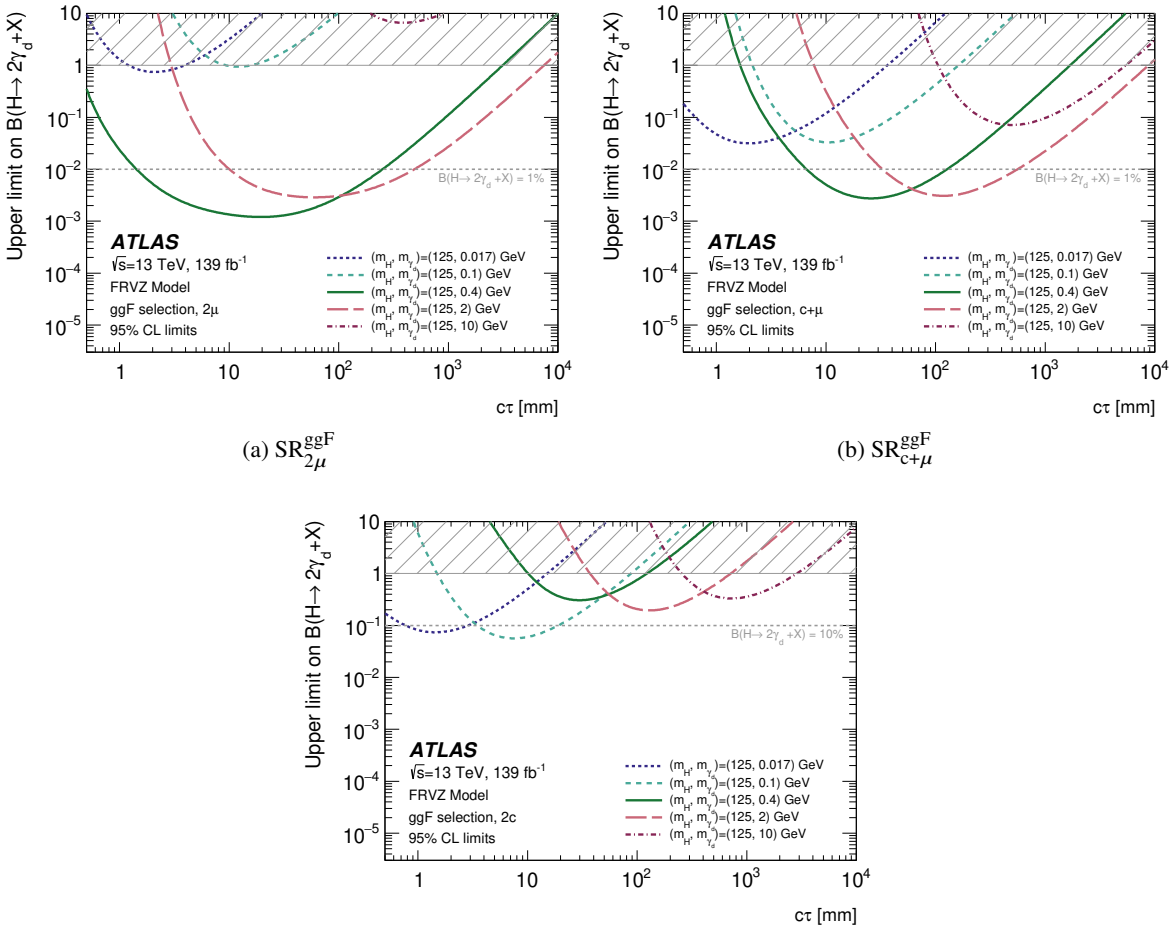

(a) $\mathrm{SR}^{\mathrm{ggF}}_{2\mu}$

(b) $\mathrm{SR}^{\mathrm{ggF}}_{\mathrm{c}+\mu}$

(c) $\mathrm{SR}^{\mathrm{ggF}}_{2\mathrm{c}}$

Figure 9: Observed 95% CL upper limits on the branching ratio (B) for the decay $H \rightarrow 2\gamma_{\mathrm{d}} + X$ and ggF selection, for different γ_{d} masses and a 125 GeV Higgs boson. The limits are shown separately for the (a) 2μ, (b) c+μ and (c) 2c search channels, assuming an FRVZ signal model. The hatched band denotes the region in which the branching ratio of $H \rightarrow 2\gamma_{\mathrm{d}} + X$ is larger than unity.

95% CL if the dark photons have a mean proper decay length between 6 mm and 30 mm and a mass between 400 MeV and 2 GeV. In the case of models leading to a total of four dark photons in the final state, the sensitivity is lower than for the $H \rightarrow 2\gamma_{\mathrm{d}} + X$ process because the large boost of dark-photon pairs from the s_{d} decays results in caloDPJs overlapping with μDPJs and failing the object-level selections. The signal region targeting decays into one caloDPJ and one μDPJ in the ggF selection was found to be the most sensitive: branching fractions above 10% are excluded at 95% CL for dark photons with a mean proper decay length between 20 mm and 50 mm and a mass between 400 MeV and 1 GeV. In order to set limits on the $pp \rightarrow H \rightarrow 2\gamma_{\mathrm{d}} + X$ process as a function of the kinetic mixing parameter ϵ and γ_{d} mass, the best-performing search channels, based on their expected sensitivity, are taken into account. In the case of FRVZ models, the mutually exclusive search channels targeting dark-photon decays into caloDPJs are statistically combined to maximise the exclusion power. The combined fit considers a product of the likelihood functions of the individual search channels with independent parameters, but with a common signal normalisation. Figure 12 considers the case of an FRVZ model with a γ_{d} mass of 100 MeV and

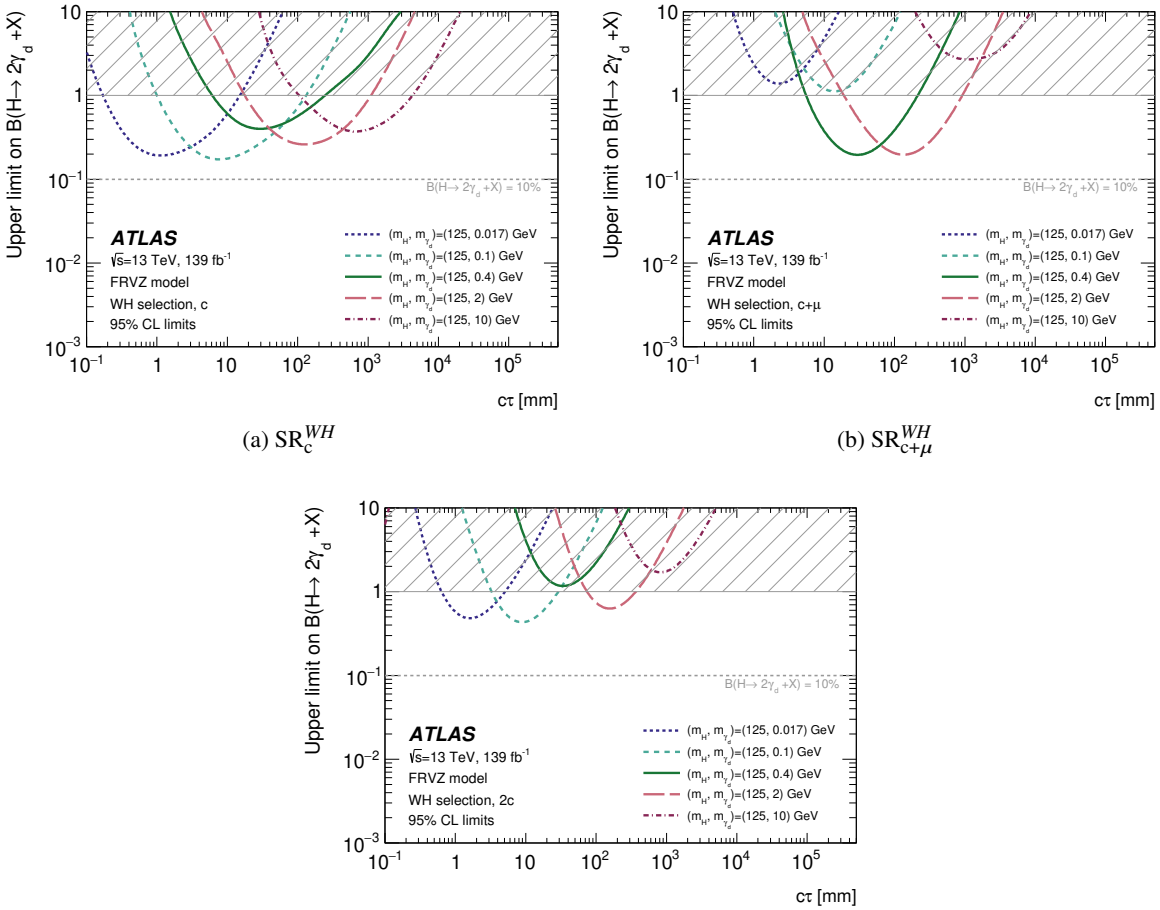

(a) $\mathrm{SR}_{\mathrm{c}}^{WH}$

(b) $\mathrm{SR}_{\mathrm{c}+\mu}^{WH}$

(c) $\mathrm{SR}_{\mathrm{2c}}^{WH}$

Figure 10: Observed 95% CL upper limits on the branching ratio (B) for the decay $H \rightarrow 2\gamma_{\mathrm{d}} + X$ and WH selection, for different γ_{d} masses and a 125 GeV Higgs boson. The limits are shown separately for the three search channels: (a) c, (b) c+μ and (c) 2c, assuming an FRVZ signal model. The hatched band denotes the region in which the branching ratio of $H \rightarrow 2\gamma_{\mathrm{d}} + X$ is larger than unity.

presents the results of the statistical combination of the $\mathrm{SR}_{\mathrm{2c}}^{\mathrm{ggF}}$, $\mathrm{SR}_{\mathrm{2c}}^{WH}$ and $\mathrm{SR}_{\mathrm{c}}^{WH}$, as 95% CL upper limits on the branching fraction of a 125 GeV Higgs boson decaying into hidden-sector particles and resulting in two dark photons. For simplicity, the $\mathrm{SR}_{\mathrm{c}+\mu}^{\mathrm{ggF}}$ is not used in the combination although it could offer an increase in sensitivity at the percent level. The figure illustrates the complementary sensitivity of the WH selection, in this case providing most of the sensitivity for dark-photon mean proper decay lengths below 2 mm or above 50 mm.

Upper limits at 90% CL[3] are also set, in the context of the FRVZ model and the HAHM vector-portal model, in terms of kinetic mixing parameter ϵ and γ_{d} mass and presented in Figure 13 for different Higgs decay branching fractions into γ_{d}, ranging from 0.1% to 10%. The limits are interpolated between different masses by branching fraction variations [9] as a function of the γ_{d} mass, corrected by a linear interpolation of the signal efficiency between adjacent available MC signal samples. For γ_{d} mass below twice the muon

[3] The limits are quoted at 90% CL in this interpretation of the results to ease the comparison with other experiments that conventionally use this CL threshold.

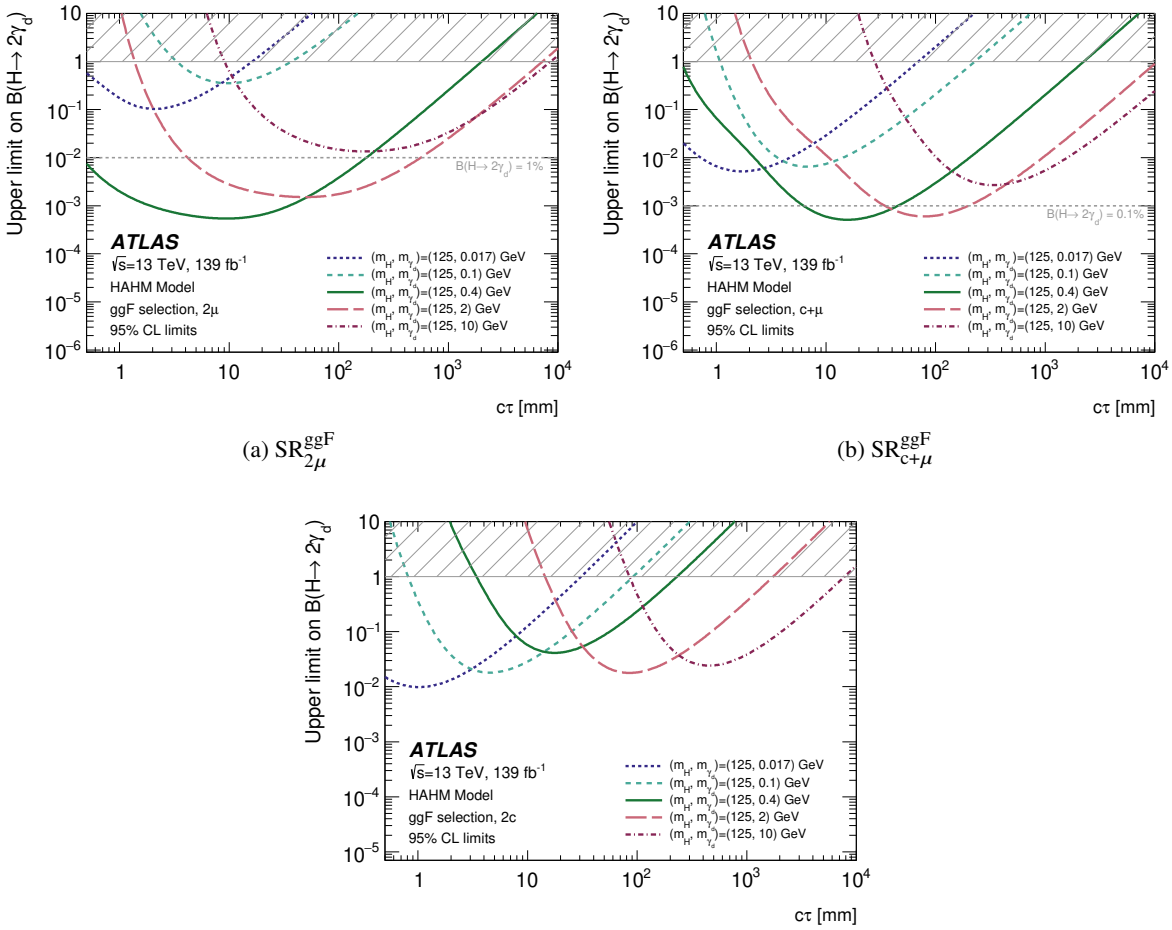

(a) $\mathrm{SR}^{\mathrm{ggF}}_{2\mu}$ (b) $\mathrm{SR}^{\mathrm{ggF}}_{\mathrm{c}+\mu}$

(c) $\mathrm{SR}^{\mathrm{ggF}}_{2\mathrm{c}}$

Figure 11: Observed 95% CL upper limits on the branching ratio (B) for the decay $H \rightarrow 2\gamma_{\mathrm{d}}$ and ggF selection, for different γ_{d} masses and a 125 GeV Higgs boson. The limits are shown separately for the (a) 2μ, (b) c+μ and (c) 2c search channels, assuming a HAHM signal model. The hatched band denotes the region in which the branching ratio of $H \rightarrow 2\gamma_{\mathrm{d}}$ is larger than unity.

mass, no coverage from μDPJ signal regions is expected, motivating a significant drop in sensitivity. The combination of the caloDPJ signal regions provides the most stringent limit in this mass range. In the mass range above twice the muon mass, only the best-performing channel for each γ_{d} mass probed is considered. The structures observed in this mass range depend on the expected γ_{d} branching ratio, where decays to QCD resonances can significantly alter the sensitivities of the different search channels.

Exclusion regions from previous ATLAS searches for dark-photon jets are shown for the displaced-decay search [14] and for the complementary prompt-decay search [17]. The contributions from the caloDPJ channels allow ATLAS to set limits for $m_{\gamma_d} < 0.1$ GeV for the first time.

This search has significantly higher sensitivity than the previous ATLAS search for light long-lived neutral particles [14], reaching a 0.1% branching ratio for a 125 GeV Higgs boson decaying into dark photons.

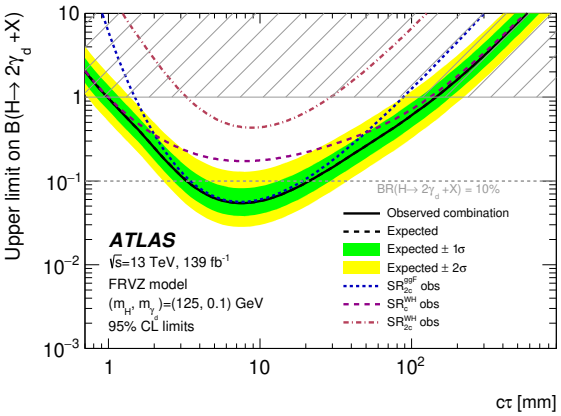

Figure 12: Exclusion limits at the 95% CL on the branching ratio (B) for the process $H \rightarrow 2\gamma_d + X$, for a γ_d mass of 100 MeV and a 125 GeV Higgs boson in an FRVZ model, as a function of the dark-photon mean proper decay length $c\tau$. The three dashed curves, taken from Figures 9(c), 10(a) and 10(c), show the individual sensitivities of the search channels targeting caloDPJs in the ggF and WH selections. The solid black curve shows the observed exclusion limit from their statistical combination, and is almost identical to the expected limit. The green and yellow bands represent $\pm 1\sigma$ and $\pm 2\sigma$ uncertainty in the expected limit. The hatched band denotes the region in which the branching ratio of $H \rightarrow 2\gamma_d + X$ is larger than unity.

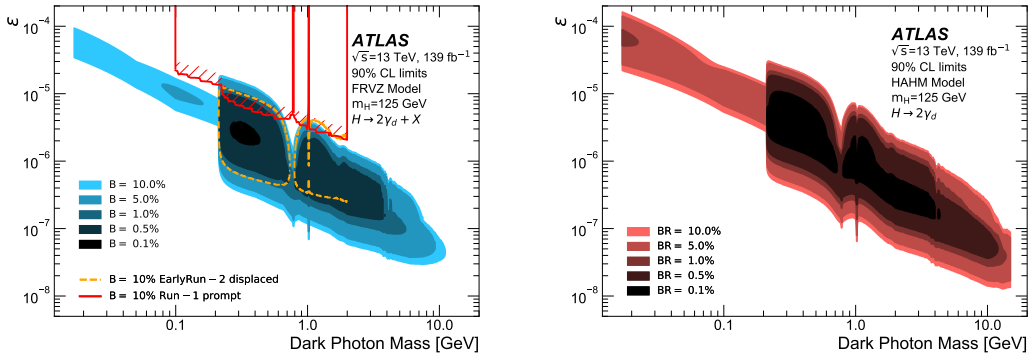

(a) FRVZ

(b) HAHM

Figure 13: The 90% CL exclusion contours of the branching ratio (B) for the decay $H \rightarrow 2\gamma_d + X$ as a function of the γ_d mass and the kinetic mixing parameter ϵ for (a) the FRVZ model and (b) the HAHM model. These limits are obtained assuming branching fractions between 0.1% and 10% for Higgs boson decays resulting in dark photons. For γ_d mass below twice the muon mass, the combination of the caloDPJ signal regions is used. The figure also shows regions excluded by the previous ATLAS searches for jets from displaced [14] (orange line) and prompt [17] (red line) decays of dark photons.

8 Conclusion

This paper presents a search for light long-lived neutral particles which decay into collimated pairs of fermions in the ATLAS detector at the LHC. Data collected from 139 fb^{-1} of $\sqrt{s}$ = 13 TeV pp collisions during 2015–2018 were analysed for evidence of long-lived dark photons from Higgs boson decays and were found to be consistent with the background prediction. Upper limits on the Higgs boson branching fraction to dark photons as a function of their mass and mean proper decay length $c\tau$ are reported, assuming SM Higgs boson production cross-sections. Branching fractions above 0.1% are excluded at 95% CL for Higgs boson decays to two dark photons with mean proper decay length between 10 mm and 250 mm and mass between 0.4 and 2 GeV. This analysis has significantly higher sensitivity than previous ATLAS searches for light long-lived neutral particles that decay to collimated pairs of fermions. The higher sensitivity is due to the addition of an event selection targeting long-lived dark photons from decays of Higgs bosons produced in association with a W boson and to the use of a larger dataset and new methodologies for reconstructing dark-photon candidates and rejecting non-collision backgrounds.

References

[1] N. Arkani-Hamed and N. Weiner, *LHC signals for a SuperUnified theory of Dark Matter*, JHEP **12** (2008) 104, arXiv: 0810.0714 [hep-ph].

[2] M. Baumgart, C. Cheung, J. T. Ruderman, L.-T. Wang and I. Yavin, *Non-abelian dark sectors and their collider signatures*, JHEP **04** (2009) 014, arXiv: 0901.0283 [hep-ph].

[3] A. Falkowski and R. Vega-Morales, *Exotic Higgs decays in the golden channel*, JHEP **12** (2014) 037, arXiv: 1405.1095 [hep-ph].

[4] D. Curtin, R. Essig, S. Gori and J. Shelton, *Illuminating dark photons with high-energy colliders*, JHEP **02** (2015) 157, arXiv: 1412.0018 [hep-ph].

[5] C. Cheung, J. T. Ruderman, L.-T. Wang and I. Yavin, *Lepton jets in (supersymmetric) electroweak processes*, JHEP **04** (2010) 116, arXiv: 0909.0290 [hep-ph].

[6] A. Falkowski, J. T. Ruderman, T. Volansky and J. Zupan, *Hidden Higgs decaying to lepton jets*, JHEP **05** (2010) 077, arXiv: 1002.2952 [hep-ph].

[7] A. Falkowski, J. T. Ruderman, T. Volansky and J. Zupan, *Discovering Higgs Boson Decays to Lepton Jets at Hadron Colliders*, Phys. Rev. Lett. **105** (2010) 241801, arXiv: 1007.3496 [hep-ph].

[8] P. Meade, M. Papucci and T. Volansky, *Dark matter sees the light*, JHEP **12** (2009) 052, arXiv: 0901.2925 [hep-ph].

[9] B. Batell, M. Pospelov and A. Ritz, *Probing a secluded U(1) at B factories*, Phys. Rev. D **79** (2009) 115008, arXiv: 0903.0363 [hep-ph].

[10] C. Cheung, J. T. Ruderman, L.-T. Wang and I. Yavin, *Kinetic mixing as the origin of a light dark-gauge-group scale*, Phys. Rev. D **80** (2009) 035008, arXiv: 0902.3246 [hep-ph].

[11] M. J. Strassler and K. M. Zurek, *Echoes of a hidden valley at hadron colliders*, Phys. Lett. B **651** (2007) 374, arXiv: hep-ph/0604261.

[12] ATLAS Collaboration, *Search for displaced muonic lepton jets from light Higgs boson decay in proton–proton collisions at* $\sqrt{s} = 7$ *TeV with the ATLAS detector*, Phys. Lett. B **721** (2013) 32, arXiv: 1210.0435 [hep-ex].

[13] ATLAS Collaboration, *Search for long-lived neutral particles decaying into lepton jets in proton–proton collisions at* $\sqrt{s} = 8$ *TeV with the ATLAS detector*, JHEP **11** (2014) 088, arXiv: 1409.0746 [hep-ex].

[14] ATLAS Collaboration, *Search for light long-lived neutral particles produced in* pp *collisions at* $\sqrt{s} = 13$ *TeV and decaying into collimated leptons or light hadrons with the ATLAS detector*, Eur. Phys. J. C **80** (2020) 450, arXiv: 1909.01246 [hep-ex].

[15] ATLAS Collaboration, *Search for WH production with a light Higgs boson decaying to prompt electron-jets in proton–proton collisions at* $\sqrt{s} = 7$ *TeV with the ATLAS detector*, New J. Phys. **15** (2013) 043009, arXiv: 1302.4403 [hep-ex].

[16] ATLAS Collaboration, *A search for prompt lepton-jets in* pp *collisions at* $\sqrt{s} = 7$ *TeV with the ATLAS detector*, Phys. Lett. B **719** (2013) 299, arXiv: 1212.5409 [hep-ex].

[17] ATLAS Collaboration,
A search for prompt lepton-jets in pp collisions at $\sqrt{s} = 8$ TeV with the ATLAS detector,
JHEP **02** (2016) 062, arXiv: 1511.05542 [hep-ex].

[18] ATLAS Collaboration, *Search for long-lived particles in final states with displaced dimuon vertices in pp collisions at $\sqrt{s} = 13$ TeV with the ATLAS detector*, Phys. Rev. D **99** (2019) 012001, arXiv: 1808.03057 [hep-ex].

[19] CDF Collaboration,
Search for anomalous production of multiple leptons in association with W and Z bosons at CDF,
Phys. Rev. D **85** (2012) 092001, arXiv: 1202.1260 [hep-ex].

[20] D0 Collaboration, *Search for Dark Photons from Supersymmetric Hidden Valleys*,
Phys. Rev. Lett. **103** (2009) 081802, arXiv: 0905.1478 [hep-ex].

[21] D0 Collaboration, *Search for Events with Leptonic Jets and Missing Transverse Energy in $p\bar{p}$ Collisions at $\sqrt{s} = 1.96$ TeV*, Phys. Rev. Lett. **105** (2010) 211802, arXiv: 1008.3356 [hep-ex].

[22] CMS Collaboration,
Search for light resonances decaying into pairs of muons as a signal of new physics,
JHEP **07** (2011) 098, arXiv: 1106.2375 [hep-ex].

[23] CMS Collaboration, *Search for a non-standard-model Higgs boson decaying to a pair of new light bosons in four-muon final states*, Phys. Lett. B **726** (2013) 564, arXiv: 1210.7619 [hep-ex].

[24] CMS Collaboration, *A search for pair production of new light bosons decaying into muons*,
Phys. Lett. B **752** (2016) 146, arXiv: 1506.00424 [hep-ex].

[25] CMS Collaboration, *Search for dark photons in decays of Higgs bosons produced in association with Z bosons in proton–proton collisions at $\sqrt{s} = 13$ TeV*, JHEP **10** (2019) 139,
arXiv: 1908.02699 [hep-ex].

[26] LHCb Collaboration, *Search for Hidden-Sector Bosons in $B^0 \to K^{*0}\mu^+\mu^-$ Decays*,
Phys. Rev. Lett. **115** (2015) 161802, arXiv: 1508.04094 [hep-ex].

[27] LHCb Collaboration, *Search for Dark Photons Produced in 13 TeV pp Collisions*,
Phys. Rev. Lett. **120** (2018) 061801, arXiv: 1710.02867 [hep-ex].

[28] J. Blümlein and J. Brunner, *New exclusion limits for dark gauge forces from beam-dump data*,
Phys. Lett. B **701** (2011) 155, arXiv: 1104.2747 [hep-ex].

[29] J. D. Bjorken, R. Essig, P. Schuster and N. Toro,
New fixed-target experiments to search for dark gauge forces, Phys. Rev. D **80** (2009) 075018,
arXiv: 0906.0580 [hep-ph].

[30] A. Bross et al., *Search for short-lived particles produced in an electron beam dump*,
Phys. Rev. Lett. **67** (1991) 2942.

[31] A1 Collaboration, *Search for Light Gauge Bosons of the Dark Sector at the Mainz Microtron*,
Phys. Rev. Lett. **106** (2011) 251802, arXiv: 1101.4091 [nucl-ex].

[32] WASA-at-COSY Collaboration, *Search for a dark photon in the $\pi^0 \to e^+e^-\gamma$ decay*,
Phys. Lett. B **726** (2013) 187, arXiv: 1304.0671 [hep-ex].

[33] APEX Collaboration, *Search for a New Gauge Boson in Electron-Nucleus Fixed-Target Scattering by the APEX Experiment*, Phys. Rev. Lett. **107** (2011) 191804, arXiv: 1108.2750 [hep-ex].

[34] M. Reece and L.-T. Wang, *Searching for the light dark gauge boson in GeV-scale experiments*,
JHEP **07** (2009) 051, arXiv: 0904.1743 [hep-ph].

[35] J. Blümlein and J. Brunner,
New exclusion limits on dark gauge forces from proton Bremsstrahlung in beam-dump data,
Phys. Lett. B **731** (2014) 320, arXiv: 1311.3870 [hep-ph].

[36] S. N. Gninenko,
Constraints on sub-GeV hidden sector gauge bosons from a search for heavy neutrino decays,
Phys. Lett. B **713** (2012) 244, arXiv: 1204.3583 [hep-ph].

[37] R. Essig, R. Harnik, J. Kaplan and N. Toro, *Discovering new light states at neutrino experiments*,
Phys. Rev. D **82** (2010) 113008, arXiv: 1008.0636 [hep-ph].

[38] HADES Collaboration, *Searching a dark photon with HADES*, Phys. Lett. B **731** (2014) 265,
arXiv: 1311.0216 [hep-ex].

[39] KLOE-2 Collaboration,
Search for a vector gauge boson in ϕ meson decays with the KLOE detector,
Phys. Lett. B **706** (2012) 251, arXiv: 1110.0411 [hep-ex].

[40] KLOE-2 Collaboration,
Limit on the production of a light vector gauge boson in ϕ meson decays with the KLOE detector,
Phys. Lett. B **720** (2013) 111, arXiv: 1210.3927 [hep-ex].

[41] BABAR Collaboration,
Search for Dimuon Decays of a Light Scalar Boson in Radiative Transitions $\Upsilon \to \gamma A^0$,
Phys. Rev. Lett. **103** (2009) 081803, arXiv: 0905.4539 [hep-ex].

[42] BABAR Collaboration, *Search for a Dark Photon in e^+e^- Collisions at BaBar*,
Phys. Rev. Lett. **113** (2014) 201801, arXiv: 1406.2980 [hep-ex].

[43] BABAR Collaboration, *Search for Long-Lived Particles in e^+e^- Collisions*,
Phys. Rev. Lett. **114** (2015) 171801, arXiv: 1502.02580 [hep-ex].

[44] Belle Collaboration, *Search for the Dark Photon and the Dark Higgs Boson at Belle*,
Phys. Rev. Lett. **114** (2015) 211801, arXiv: 1502.00084 [hep-ex].

[45] Belle Collaboration,
Search for a dark vector gauge boson decaying to $\pi^+\pi^-$ using $\eta \to \pi^+\pi^-\gamma$ decays,
Phys. Rev. D **94** (2016) 092006, arXiv: 1609.05599 [hep-ex].

[46] BESIII Collaboration, *Measurement of $\mathcal{B}(J/\psi \to \eta' e^+e^-)$ and search for a dark photon*,
Phys. Rev. D **99** (2019) 012013, arXiv: 1809.00635 [hep-ex].

[47] BESIII Collaboration, *Dark photon search in the mass range between 1.5 and 3.4 GeV/c^2*,
Phys. Lett. B **774** (2017) 252, arXiv: 1705.04265 [hep-ex].

[48] M. Pospelov, *Secluded U(1) below the weak scale*, Phys. Rev. D **80** (2009) 095002,
arXiv: 0811.1030 [hep-ph].

[49] H. Davoudiasl, H.-S. Lee and W. J. Marciano, *Dark side of Higgs diphoton decays and muon $g-2$*,
Phys. Rev. D **86** (2012) 095009, arXiv: 1208.2973 [hep-ph].

[50] M. Endo, K. Hamaguchi and G. Mishima,
Constraints on hidden photon models from electron $g-2$ and hydrogen spectroscopy,
Phys. Rev. D **86** (2012) 095029, arXiv: 1209.2558 [hep-ph].

[51] J. H. Chang, R. Essig and S. D. McDermott, *Supernova 1987A constraints on sub-GeV dark sectors, millicharged particles, the QCD axion, and an axion-like particle*, JHEP **09** (2018) 051,
arXiv: 1803.00993 [hep-ph].

[52] H. K. Dreiner, J.-F. Fortin, C. Hanhart and L. Ubaldi,
Supernova constraints on MeV dark sectors from e^+e^- annihilations,
Phys. Rev. D **89** (2014) 105015, arXiv: 1310.3826 [hep-ph].

[53] ATLAS Collaboration, *The ATLAS Experiment at the CERN Large Hadron Collider*,
JINST **3** (2008) S08003.

[54] ATLAS Collaboration, *Performance of the ATLAS trigger system in 2015*,
Eur. Phys. J. C **77** (2017) 317, arXiv: 1611.09661 [hep-ex].

[55] ATLAS Collaboration, *The ATLAS Collaboration Software and Firmware*,
ATL-SOFT-PUB-2021-001, 2021, URL: https://cds.cern.ch/record/2767187.

[56] ATLAS Collaboration,
ATLAS data quality operations and performance for 2015–2018 data-taking,
JINST **15** (2020) P04003, arXiv: 1911.04632 [physics.ins-det].

[57] ATLAS Collaboration, *Performance of the ATLAS muon triggers in Run 2*,
JINST **15** (2020) P09015, arXiv: 2004.13447 [hep-ex].

[58] ATLAS Collaboration, *Performance of electron and photon triggers in ATLAS during LHC Run 2*,
Eur. Phys. J. C **80** (2020) 47, arXiv: 1909.00761 [hep-ex].

[59] L. Evans and P. Bryant, *LHC Machine*, JINST **3** (2008) S08001.

[60] J. Alwall et al., *The automated computation of tree-level and next-to-leading order differential cross sections, and their matching to parton shower simulations*, JHEP **07** (2014) 079,
arXiv: 1405.0301 [hep-ph].

[61] T. Sjöstrand, S. Mrenna and P. Skands, *A brief introduction to PYTHIA 8.1*,
Comput. Phys. Commun. **178** (2008) 852, arXiv: 0710.3820 [hep-ph].

[62] R. D. Ball et al., *Parton distributions with LHC data*, Nucl. Phys. B **867** (2013) 244,
arXiv: 1207.1303 [hep-ph].

[63] M. Cepeda et al., *Report from Working Group 2: Higgs Physics at the HL-LHC and HE-LHC*,
CERN Yellow Rep. Monogr. **7** (2019) 221, ed. by A. Dainese et al.,
arXiv: 1902.00134 [hep-ph].

[64] C. Anastasiou et al.,
High precision determination of the gluon fusion Higgs boson cross-section at the LHC,
JHEP **05** (2016) 058, arXiv: 1602.00695 [hep-ph].

[65] D. de Florian et al.,
Handbook of LHC Higgs Cross Sections: 4. Deciphering the Nature of the Higgs Sector, (2016),
arXiv: 1610.07922 [hep-ph].

[66] O. Brein, A. Djouadi and R. Harlander,
NNLO QCD corrections to the Higgs-strahlung processes at hadron colliders,
Phys. Lett. B **579** (2004) 149, arXiv: hep-ph/0307206.

[67] ATLAS Collaboration,
Constraining the dark sector with the monojet signature in the ATLAS experiment,
ATL-PHYS-PUB-2021-020, 2021, URL: https://cds.cern.ch/record/2772627.

[68] T. Sjöstrand et al., *An introduction to PYTHIA 8.2*, Comput. Phys. Commun. **191** (2015) 159,
arXiv: 1410.3012 [hep-ph].

[69] T. Gleisberg et al., *Event generation with SHERPA 1.1*, JHEP **02** (2009) 007, arXiv: 0811.4622 [hep-ph].

[70] R. D. Ball et al., *Parton distributions for the LHC run II*, JHEP **04** (2015) 040, arXiv: 1410.8849 [hep-ph].

[71] S. Frixione, P. Nason and C. Oleari, *Matching NLO QCD computations with parton shower simulations: the POWHEG method*, JHEP **11** (2007) 070, arXiv: 0709.2092 [hep-ph].

[72] ATLAS Collaboration, *ATLAS Pythia 8 tunes to 7 TeV data*, ATL-PHYS-PUB-2014-021, 2014, URL: https://cds.cern.ch/record/1966419.

[73] P. Golonka and Z. Was, *PHOTOS Monte Carlo: a precision tool for QED corrections in Z and W decays*, Eur. Phys. J. C **45** (2006) 97, arXiv: hep-ph/0506026.

[74] J. Gao et al., *CT10 next-to-next-to-leading order global analysis of QCD*, Phys. Rev. D **89** (2014) 033009, arXiv: 1302.6246 [hep-ph].

[75] J. Pumplin et al., *New Generation of Parton Distributions with Uncertainties from Global QCD Analysis*, JHEP **07** (2002) 012, arXiv: hep-ph/0201195.

[76] ATLAS Collaboration, *The ATLAS Simulation Infrastructure*, Eur. Phys. J. C **70** (2010) 823, arXiv: 1005.4568 [physics.ins-det].

[77] GEANT4 Collaboration, S. Agostinelli et al., *GEANT4 – a simulation toolkit*, Nucl. Instrum. Meth. A **506** (2003) 250.

[78] ATLAS Collaboration, *The Pythia 8 A3 tune description of ATLAS minimum bias and inelastic measurements incorporating the Donnachie–Landshoff diffractive model*, ATL-PHYS-PUB-2016-017, 2016, URL: https://cds.cern.ch/record/2206965.

[79] ATLAS Collaboration, *Vertex Reconstruction Performance of the ATLAS Detector at* $\sqrt{s} = 13$ *TeV*, ATL-PHYS-PUB-2015-026, 2015, URL: https://cds.cern.ch/record/2037717.

[80] ATLAS Collaboration, *Performance of missing transverse momentum reconstruction with the ATLAS detector in the first proton–proton collisions at* $\sqrt{s} = 13$ *TeV*, ATL-PHYS-PUB-2015-027, 2015, URL: https://cds.cern.ch/record/2037904.

[81] ATLAS Collaboration, E_T^{miss} *performance in the ATLAS detector using 2015–2016 LHC pp collisions*, ATLAS-CONF-2018-023, 2018, URL: https://cds.cern.ch/record/2625233.

[82] ATLAS Collaboration, *Topological cell clustering in the ATLAS calorimeters and its performance in LHC Run 1*, Eur. Phys. J. C **77** (2017) 490, arXiv: 1603.02934 [hep-ex].

[83] ATLAS Collaboration, *Properties of jets and inputs to jet reconstruction and calibration with the ATLAS detector using proton–proton collisions at* $\sqrt{s} = 13$ *TeV*, ATL-PHYS-PUB-2015-036, 2015, URL: https://cds.cern.ch/record/2044564.

[84] M. Cacciari, G. P. Salam and G. Soyez, *The anti-k_t jet clustering algorithm*, JHEP **04** (2008) 063, arXiv: 0802.1189 [hep-ph].

[85] M. Cacciari, G. P. Salam and G. Soyez, *FastJet user manual*, Eur. Phys. J. C **72** (2012) 1896, arXiv: 1111.6097 [hep-ph].

[86] ATLAS Collaboration, *Jet energy scale measurements and their systematic uncertainties in proton–proton collisions at $\sqrt{s}$ = 13 TeV with the ATLAS detector*, Phys. Rev. D **96** (2017) 072002, arXiv: 1703.09665 [hep-ex].

[87] ATLAS Collaboration, *Performance of pile-up mitigation techniques for jets in pp collisions at $\sqrt{s}$ = 8 TeV using the ATLAS detector*, Eur. Phys. J. C **76** (2016) 581, arXiv: 1510.03823 [hep-ex].

[88] ATLAS Collaboration, *Selection of jets produced in* 13 *TeV proton–proton collisions with the ATLAS detector*, ATLAS-CONF-2015-029, 2015, URL: https://cds.cern.ch/record/2037702.

[89] ATLAS Collaboration, *Optimisation and performance studies of the ATLAS b-tagging algorithms for the 2017-18 LHC run*, ATL-PHYS-PUB-2017-013, 2017, URL: https://cds.cern.ch/record/2273281.

[90] ATLAS Collaboration, *ATLAS b-jet identification performance and efficiency measurement with $t\bar{t}$ events in pp collisions at $\sqrt{s}$ = 13 TeV*, Eur. Phys. J. C **79** (2019) 970, arXiv: 1907.05120 [hep-ex].

[91] ATLAS Collaboration, *Measurement of b-tagging efficiency of c-jets in $t\bar{t}$ events using a likelihood approach with the ATLAS detector*, ATLAS-CONF-2018-001, 2018, URL: https://cds.cern.ch/record/2306649.

[92] ATLAS Collaboration, *Calibration of light-flavour b-jet mistagging rates using ATLAS proton–proton collision data at $\sqrt{s}$ = 13 TeV*, ATLAS-CONF-2018-006, 2018, URL: https://cds.cern.ch/record/2314418.

[93] ATLAS Collaboration, *Electron and photon performance measurements with the ATLAS detector using the 2015–2017 LHC proton–proton collision data*, JINST **14** (2019) P12006, arXiv: 1908.00005 [hep-ex].

[94] ATLAS Collaboration, *Muon reconstruction and identification efficiency in ATLAS using the full Run 2 pp collision data set at $\sqrt{s}$ = 13 TeV*, Eur. Phys. J. C **81** (2021) 578, arXiv: 2012.00578 [hep-ex].

[95] ATLAS Collaboration, *Muon reconstruction performance of the ATLAS detector in proton–proton collision data at $\sqrt{s}$ = 13 TeV*, Eur. Phys. J. C **76** (2016) 292, arXiv: 1603.05598 [hep-ex].

[96] ATLAS Collaboration, *Monitoring and data quality assessment of the ATLAS liquid argon calorimeter*, JINST **9** (2014) P07024, arXiv: 1405.3768 [hep-ex].

[97] Y. L. Dokshitzer, G. D. Leder, S. Moretti and B. R. Webber, *Better jet clustering algorithms*, JHEP **08** (1997) 001, arXiv: hep-ph/9707323 [hep-ph].

[98] M. Abadi et al., *TensorFlow: Large-Scale Machine Learning on Heterogeneous Systems*, (2016), arXiv: 1603.04467 [cs.DC].

[99] ATLAS Collaboration, *Triggers for displaced decays of long-lived neutral particles in the ATLAS detector*, JINST **8** (2013) P07015, arXiv: 1305.2284 [hep-ex].

[100] ATLAS Collaboration, *Performance of the ATLAS Level-1 topological trigger in Run 2*, Eur. Phys. J. C **82** (2021) 7, arXiv: 2105.01416 [hep-ex].

[101] ATLAS Collaboration, *Search for neutral long-lived particles in pp collisions at $\sqrt{s} = 13$ TeV that decay into displaced hadronic jets in the ATLAS calorimeter*, (2022), arXiv: 2203.01009 [hep-ex].

[102] ATLAS Collaboration, *Measurement of the Inelastic Proton–Proton Cross Section at $\sqrt{s} = 13$ TeV with the ATLAS Detector at the LHC*, Phys. Rev. Lett. **117** (2016) 182002, arXiv: 1606.02625 [hep-ex].

[103] ATLAS Collaboration, *Luminosity determination in pp collisions at $\sqrt{s} = 13$ TeV using the ATLAS detector at the LHC*, ATLAS-CONF-2019-021, 2019, URL: https://cds.cern.ch/record/2677054.

[104] G. Avoni et al., *The new LUCID-2 detector for luminosity measurement and monitoring in ATLAS*, JINST **13** (2018) P07017.

[105] A. L. Read, *Presentation of search results: the CL_S technique*, J. Phys. G **28** (2002) 2693.

[106] G. Cowan, K. Cranmer, E. Gross and O. Vitells, *Asymptotic formulae for likelihood-based tests of new physics*, Eur. Phys. J. C **71** (2011) 1554, arXiv: 1007.1727 [physics.data-an], Erratum: Eur. Phys. J. C **73** (2013) 2501.